

Analyzing the Distribution and Variation of Suspended Particulate Matter in the Yellow River Estuary (YRE) using Landsat 8 OLI

Jin Li

Inner Mongolia University

Yanling Hao (✉ haoyl@imu.edu.cn)

Inner Mongolia University

Zhuangzhuang Zhang

Inner Mongolia University

Zhipeng Li

Inner Mongolia University

Ruihong Yu

Inner Mongolia University

Ying Sun

Hohhot ecological environment monitoring station of inner Mongolia

Research article

Keywords: Yellow River Estuary (YRE), Suspended Particulate Matter (SPM), Landsat 8 OLI, remote sensing inversion

Posted Date: December 10th, 2020

DOI: <https://doi.org/10.21203/rs.3.rs-121823/v1>

License: © ⓘ This work is licensed under a Creative Commons Attribution 4.0 International License.

[Read Full License](#)

1 Analyzing the distribution and variation of suspended particulate matter in the Yellow River Estuary
2 (YRE) using Landsat 8 OLI

3 Jin Li¹, Yanling Hao^{1,*}, Zhuangzhuang Zhang¹, Zhipeng Li¹, Ruihong Yu^{1,2}, Ying Sun³

4 ¹ Inner Mongolia Key Laboratory of River and Lake Ecology, School of Ecology and Environment, Inner Mongolia
5 University, 010021, China

6 ² Ministry of Education Key Laboratory of Ecology and Resource Use of the Mongolian Plateau, 010021, China

7 ³ Hohhot ecological environment monitoring station of Inner Mongolia, 010030, China

8 **Abstract**

9 Yellow River Estuary (YRE) as well as its adjacent coastal areas are famous for its high concentration of
10 Suspended Particulate Matter (SPM). The distribution of SPM and its variations in the estuary area promoted the
11 carbon, oxygen and nutrient cycles in coastal areas and nearby sea areas. This study took advantage of Landsat 8
12 Operational Land Imager (Landsat 8 OLI) data to estimate SPM in the YRE from 2013 to 2019. Remote sensing
13 reflectance (R_{rs}) measured by Landsat 8 OLI has been proved to be effective through cross-validate with
14 Geostationary Ocean Color Imager (GOCI). A simple empirical algorithm (NIR band ratio green band and add red
15 band) was developed to map the SPM distribution and concentration, with the APD 33.12% and R^2 0.93 based on
16 in-situ data. Annual average distribution of SPM shows that highly turbid areas with SPM greater than 10^3 mg/L are
17 mostly found surrounding the estuary of Yellow River, in the northwest part of the Laizhou Bay and south part of
18 Bohai bay. High variations of SPM distributions are consistent with high SPM, and vice versa. The influences of
19 river runoff is mainly concentrated in the estuary area, and outside 4.5 km the variability of SPM effected by river
20 discharge is not obvious. Significant difference is observed in seasonal SPM distribution. Higher SPM in winter is
21 observed both in range and intensity compared to summer. Significant seasonal variations are mainly controlled by
22 sediment resuspension processes driven by wind-wave forces. The results of this study indicate that Landsat8 OLI
23 is an effective mean to retrieve SPM in YRE and its adjacent areas.

24 **Key words: Yellow River Estuary (YRE), Suspended Particulate Matter (SPM), Landsat 8 OLI, remote**
25 **sensing inversion**

26 **1. Introduction**

27 The Yellow river, well-known for its high Suspended Particulate Matter (SPM) in the world and for its
28 frequently shifting courses in the low reaches ([Milliman & Meade, 1983](#)). Historically, the yellow river transported
29 about $5.74 \times 10^{10} \text{m}^3$ of freshwater (corresponding approximately 50–60% of freshwater entering the Bohai) and 1.64×10^9
30 tons of sediment (about more than 90% of sediment entering the Bohai Sea) annually ([Fan & Huang, 2008](#); [Pang et al.,](#)
31 [2000](#); [Qiu et al., 2017](#)). Coastal waters are often characterized by high concentration of SPM due to terrestrial
32 inputs and sediment resuspension. The river outflow carries SPM including inorganic and organic matter, mud sand,
33 microorganisms into the Bohai Sea. The Yellow River Estuary (YRE) and its adjacent coastal areas are famous for
34 high SPM and complex hydrodynamics which are affected by physical, biogeochemical and human activities
35 ([Cloern, 1987](#); [Li et al., 2018](#); [Wei et al., 2016](#)). The dynamics of SPM directly affect the transport of carbon,
36 nutrients, pollutants, and other materials ([Ilyina et al., 2006](#)). High SPM could affect the transparency, turbidity and
37 water color through hindering the transmission of light in the water ([Wang et al., 2017](#); [Wu et al., 2014](#)). Therefore,
38 monitoring the dynamics is of great interest and importance in the YRE and in coastal regions and nearby seas. The
39 large spatial and temporal variability of SPM, however, makes it difficult to synoptically map such matter using
40 traditional field sampling methods. Satellite remote sensing can overcome this shortage according to its large-scale
41 and real time observation, so it can be used to quickly estimate SPM in coastal and estuarine environments ([Mao et](#)
42 [al., 2012](#)).

43 Remote sensing techniques have been widely applied to obtain the spatiotemporal information of SPM since
44 the first Landsat satellite's launch in 1972. Then, sensors such as the Sea-viewing Wide Field-of-view Sensor
45 (SeaWiFS), the Moderate Resolution Imaging Spectroradiometer (MODIS), the Medium Resolution Imaging
46 Spectrometer (MERIS), Geostationary Ocean Color Imager (GOCI) and Landsat have been applied to retrieve SPM
47 successfully ([He et al., 2013](#); [Mélin et al., 2007](#); [Petus et al., 2010](#); [Ritchie et al., 2003](#); [Wang & Jiang, 2008](#); [Zhang
48 et al., 2014](#)). In contrast, Landsat 8 Operational Land Imager (L8/OLI) data, including an additional shorter blue
49 band, a narrower near-infrared band, a 12 bit radiometric resolution, and higher signal-to-noise ratios, may improve
50 the capacities of monitoring high turbid waters ([Olmanson et al., 2016](#)). In addition to these ascendancy, Landsat 8
51 OLI with high spatial resolution (30m) improved capabilities of data and so improved capacities to monitor high
52 turbid waters. Landsat 8 OLI has increasingly been used for estuary SPM monitoring due to the advantages of
53 terrestrial satellite series satellite datasets, including public accessibility, gradual (30m) and long-term availability
54 ([Luan et al., 2017](#); [Pan et al., 2018](#); [Qiu et al., 2017](#); [Zhang et al., 2014](#)).

55 The retrievals of SPM are usually exhibited in analytic, semi-analytic and empirical methods ([Binding et al.,
56 2005](#)). A large number of empirical algorithms have been developed in different estuaries and coastal zones based
57 on the relationship between the SPM and remote sensing reflectance ([Curran et al., 1987](#); [Larouche &
58 Boyer-Villemaire, 2010](#)). However, such empirical methods highly depend on in-situ datasets and therefore have
59 regional applicability characteristics ([He et al., 2013](#)).

60 The purposes of this study are to analyze the spatiotemporal distribution of the SPM derived from Landsat 8
61 OLI in the YRE, so as to provide reference data for studying the distribution of sediment and the influencing factors
62 of SPM transport. The paper was organized as follows. In-situ data and remotely sensed data used in this study are
63 described along with the SPM retrieval model and its calibration in Section 2. The accuracy of the atmospheric
64 correction algorithm and the model is assessed through cross-validation with GOCI in Section 3, and the average
65 annual distribution of SPM from 2013 to 2019 were also displayed. In section 4, Landsat 8 OLI was used to retrieve
66 monthly and seasonal variations of SPM, and the spatial distribution were characterized to analyze the factors
67 affecting the distribution of SPM. Finally, the summary and conclusions were given in Section 5.

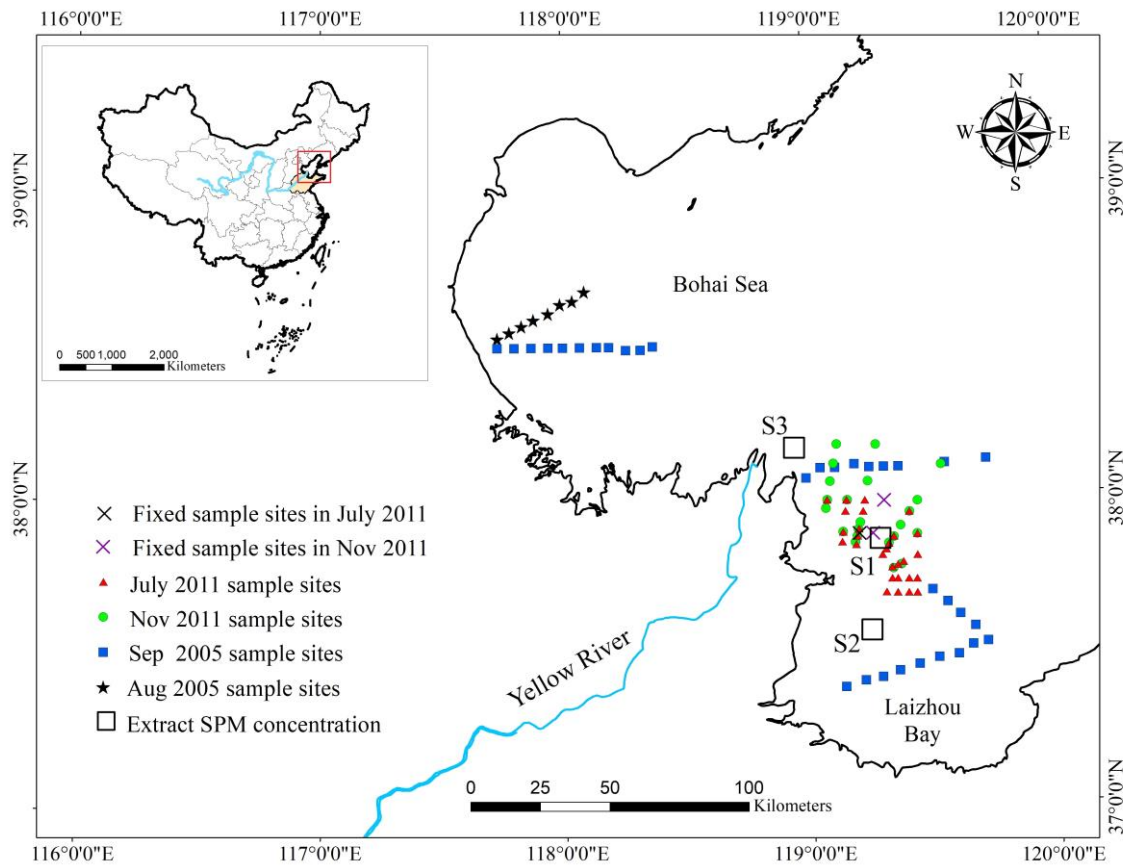
68 **2. Data and Methods**

69 **2.1 Study area**

70 The YRE is a semi-closed area located southwest of the Bohai Sea in China, with an average depth of about
71 18m ([Ruddick et al., 2012](#)). The water body in the YRE is a typical case-II water with high suspended sediment
72 concentration along with obvious regional and seasonal characteristics ([Zhao et al., 2014](#)). Affected by river input
73 and runoff, the YRE has extensive organic sediments and inorganic deposits, forming its Inherent Optical properties
74 (IOP) ([Zhao et al., 2014](#)). The study area was focused on the Yellow River estuary and adjacent waters (Fig. 1).

75 **2.2 Satellite data**

76 Landsat 8 OLI was successfully launched by NASA on February 11, 2013. Operational Land Imager (OLI)
77 image width is 185×185km, with an additional shorter blue band, a narrower near-infrared band, a 12 bit
78 radiometric resolution, and higher signal-to-noise ratios. OLI provided quantified, improved signal-to-noise ratio
79 (SNR) in a 12-bit dynamic range with full coverage every 16 days. All Landsat 8 OLI images (from May 2013 to
80 August 2019) in this study area (row 121, path 34) were download from the United States Geological Survey
81 (USGS) (<https://www.usgs.gov/products/data-and-tools/data-and-tools-topics>). Through careful selection, a total of
82 53 Landsat 8 OLI images with less than 20% cloud covered were obtained. Atmospheric corrections were
83 processed using the short-wave infrared (SWIR) algorithm method ([Qing et al., 2019](#); [Vanhellemont & Ruddick,
84 2014, 2015](#)) and the FLAASH algorithm which embed into ENVI image processing software.



85
 86 Fig. 1. Sampling site map during three cruises (The red solid triangle represents sample sites in July 2011; the
 87 green solid dot represents sample sites in November 2011; the blue polygon represents sample sites in Aug
 88 2005; the black solid star represents sample sites in Sep 2005; the cross represents three fixed sample sites
 89 (black cross represents in July 2011, and the purple cross was in Nov 2011); the black hollow square boxes of
 90 40×40 pixels for characterizing SPM (S1, S2, S3).

91 **2.3 In-situ data**

92 The data of this study were collected by three oceanographic cruises in the YRE and its vicinity in 2005 and
 93 2011 (the observation stations in Fig. 1). Both the remote sensing reflectance (R_{rs}) and SPM were measured in the
 94 three cruises over the YRE and 130 group of data including R_{rs} and SPM were included. In the following research,
 95 all the data were arranged according to the same concentration gradient. Two-thirds of them were used to establish
 96 the SPM retrieval algorithm, and the remaining data was used to verify the correctness of the algorithm. The
 97 measurement methods for R_{rs} and SPM are described as follows.

98 **2.3.1 Measurement of SPM**

99 SPM measurements used standard gravimetric methods, including water sample collection, filter preparation,
 100 on-site filtration, and laboratory weighing (Zhang et al., 2014). Using sampling bottles to collect water samples
 101 from the top several centimeters of the water surface and completing optical measurement at the same time. Before
 102 filtration, the filter is repeatedly dried, cooled, and weighed until the weight changes by no more than 0.2mg. The
 103 water samples were filtered through Whatman GF/F filters (diameter 47 mm, pore size 0.45 μm), then placed in the
 104 silica gel drier for 6–8h. Finally, the filtered membranes were re-weighed to obtain the SPM and stored in a
 105 refrigerator for on-shore analysis.

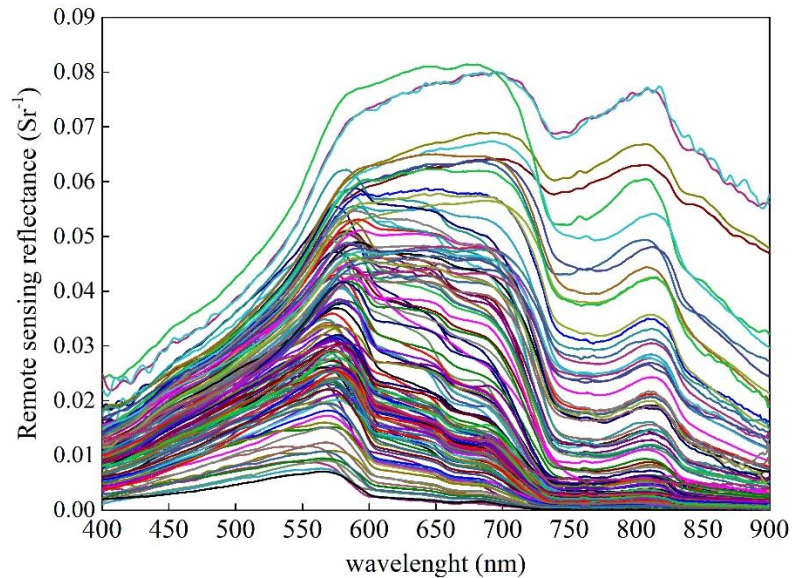
106 2.3.2 Measurement of remote sensing reflectance

107 Remote sensing reflectance (R_{rs}) were measured using an ASD Field Spec 4 with a spectral range of
108 350-2500nm and the absolute radiance calibration of detectors was performed before each cruise. In order to avoid
109 and minimize the effects of sunlight reflectance and ship shadows, the zenith and azimuth angles viewing from the
110 water surface are about 40° and 135° respectively (Pei et al., 2015). The radiance of water surface, the plate and the
111 sky were received by ASD detector. The reflections from superstructures, ship wakes, associated foam patches, and
112 whitecaps should be considered when selecting measurement locations. In addition, the sun light plays a vital role,
113 so the observation time is generally chosen between 9 am and 3 pm every day. The R_{rs} calculation method used was
114 detailed in formula (1) and the measured R_{rs} was shown in Fig. 2.

115 The measured R_{rs} is calculated using Eq (1):

$$R_{rs} = \frac{L_{sw} - \rho L_{sky}}{\pi L_p / \rho_p} \quad (1)$$

116 Where L_{sw} is the radiance of water surface; L_{sky} is the radiance of sky; L_p is the radiance of plate; ρ is a
117 fixed value and its value is generally between 0.022–0.05 (Mobley, 1999).

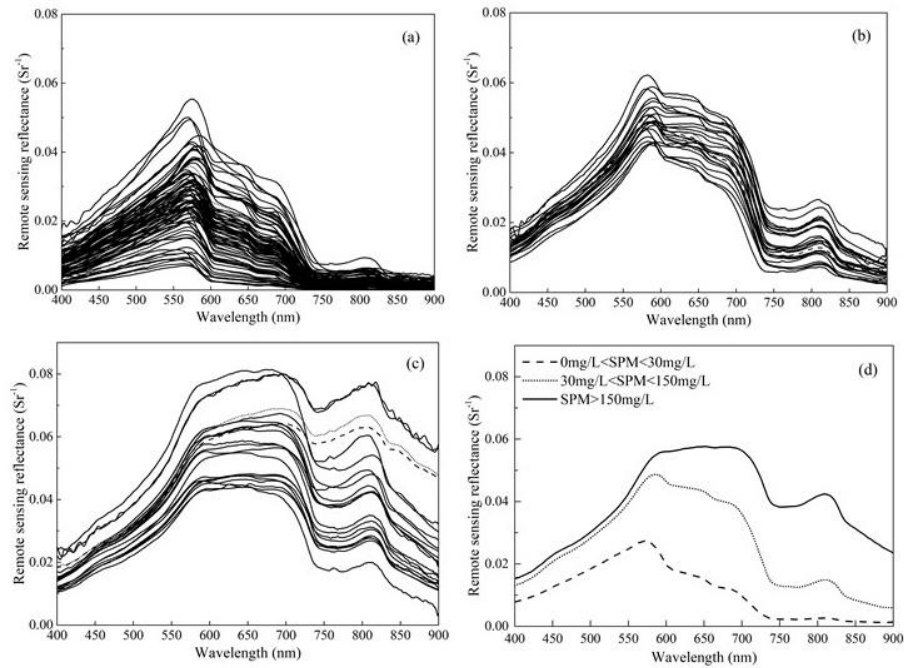


118
119 Fig. 2. The remote sensing reflectance during three cruise.

120 2.4 SPM retrieval model

121 2.4.1 Variation of the R_{rs} with different SPM range in the YRE

122 The study divided all the SPM into three concentration range including low turbidity water (with
123 $SPM < 30\text{mg/L}$), moderate turbidity water ($30\text{mg/L} < SPM < 150\text{mg/L}$) and high turbidity water ($SPM > 150\text{mg/L}$). Fig.
124 3 indicate the remote sensing reflectance of different SPM range.



125

126 Fig. 3. R_{rs} and mean R_{rs} of different SPM range. (a) R_{rs} in the low turbidity water (with $0\text{mg/L} < \text{SPM} < 30\text{mg/L}$); (b)
 127 R_{rs} in the moderate turbidity water (with $30\text{mg/L} < \text{SPM} < 150\text{mg/L}$); (c) R_{rs} in the high turbidity water (with
 128 $\text{SPM} > 150\text{mg/L}$); (d) Mean R_{rs} in three different SPM range.

129 As Fig. 3(a) shows, the values of the R_{rs} increase from blue to green band, reaching the peak at 570 nm in the
 130 low turbidity water. The peak of R_{rs} at 570nm is mainly due to high backscattering from SPM. The values decrease
 131 quickly in the range of 570-600 nm, and finally end with the minimum at the near infrared band. The downslope
 132 (from 570 to 600 nm) is generally steeper than the upslope (from the blue to green band).

133 For moderate turbidity water (Fig. 3(b)), the shape of spectral characteristic curves is similar to those in the
 134 low turbidity water in the blue and green bands. The spectral value decreases from 570nm to 750nm, and the R_{rs}
 135 increased between 600nm and 700nm compared to low turbidity water with its value almost among 0.023 S_r^{-1} to
 136 0.057 S_r^{-1} . In addition, a small peak appeared at 810nm with R_{rs} among 0.007 S_r^{-1} to 0.026 S_r^{-1} .

137 Fig. 3(c) showed the R_{rs} in the high turbidity water, and the R_{rs} were at a high level compared to the low and
 138 moderate turbidity water. A reflection peak platform appeared from 550nm to 700nm. The R_{rs} at 570nm is normally
 139 higher than that at 700nm for low and moderate turbidity water, and this phenomenon is reversed for high turbidity
 140 water, because R_{rs} at 570 nm tends to saturate while SPM increases. A more widely peak at 810nm with R_{rs} among
 141 0.02 S_r^{-1} to 0.08 S_r^{-1} become more obvious compared to the first two spectral curves.

142 Fig. 3(d) showed the mean R_{rs} in three different SPM range, and the value of R_{rs} increased with the
 143 concentration of SPM. The R_{rs} of the visible and near-infrared spectral regions vary widely in different SPM ranges
 144 which is similar to the results published in other turbid waters ([M. Zhang et al., 2010](#)).

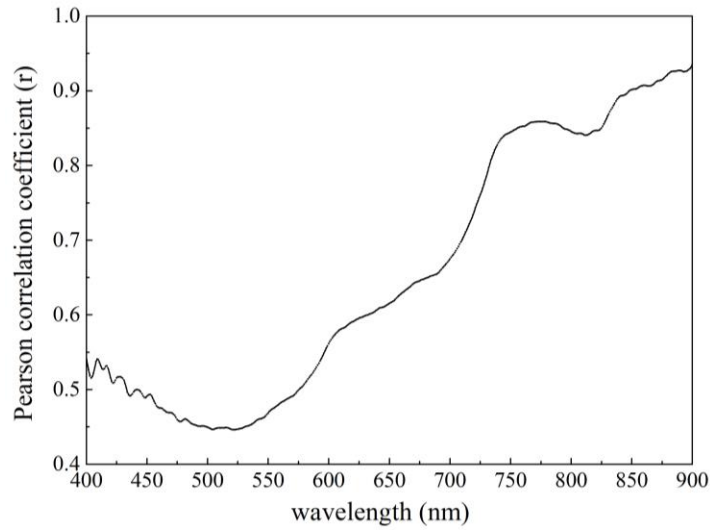
145 2.4.2 The selection of sensitive wavelength

146 In previous studies, many empirical algorithms were developed to retrieve SPM. [Zhang et al. \(2014\)](#) used a
 147 single parameter linear model establishing a retrieval algorithm to map SPM in the YRE by Landsat TM/ETM+.
 148 [Qiu \(2013\)](#) suggested taking advantage of power functions and quadratic polynomials to retrieve SPM in the YRE.
 149 [Doxaran et al. \(2009\)](#) applied the 895nm and 685nm to develop the algorithm in Gironde Estuary in which the SPM
 150 was similar to the Yellow River Estuary. [Y. Zhang et al. \(2010\)](#) used the ratio of 470nm and 645nm to establish a
 151 quadratic equation to retrieve the SPM in Taihu Lake, China. [Hu et al. \(2004\)](#) created bands difference algorithm to

152 analyze total suspended sediment concentration using Modis at Tampa Bay, Florida Bay. The study obtained spectra
 153 ranging 400nm to 900nm, and attempted to establish a new model to retrieve SPM in the YRE. Each band has
 154 different response to different concentration of SPM. So it's necessary to explore the correlation between SPM and
 155 wavelength to find the sensitive bands to SPM. The correlation coefficient between the R_{rs} and SPM can be
 156 calculated by Pearson correlation coefficient equation which is described as Eq (2):

$$157 \quad r = \frac{\sum(x-\bar{x})(y_{\lambda}-\bar{y}_{\lambda})}{\sqrt{\sum(x-\bar{x})^2}\sqrt{\sum(y_{\lambda}-\bar{y}_{\lambda})^2}} \quad (2)$$

158 where the x is SPM, \bar{x} is the mean SPM. y_{λ} is the R_{rs} of wavelength, and \bar{y}_{λ} is the mean R_{rs} of
 159 wavelength. r represents the correlation coefficient. Fig. 3 shows the correlation coefficient between R_{rs} and SPM
 160 from 400nm to 900 nm.



161
 162 Fig. 4. The correlation coefficient of the R_{rs} with SPM at different wavelengths.

163 Correlation coefficients between remote sensing reflectance and SPM increased significantly with increasing
 164 wavelength from 520nm to 900nm. r of near-infrared band is higher than that in the red band with its value more
 165 than 0.8. The reason for this phenomenon is that the signals reflected by high turbid water tend to saturate in visible
 166 light range while the saturation effect reduce relatively in the near-infrared spectral region (Doxaran et al., 2002).
 167 According to the central wavelength setting of Landsat 8 OLI and the correlation coefficient trend, 561nm, 655nm
 168 and 865nm bands are selected to establish SPM retrieval algorithms in the YRE. Many different forms of empirical
 169 formulas including single band and the combinations of different bands and band ratios were established in this
 170 study. The performance of algorithms was evaluated by the coefficient of determination (R^2) and the Average
 171 Percentage Difference (APD). The R^2 and APD calculation method are showed in Eq (3) and (4) respectively:

$$172 \quad R^2 = \frac{\sum_1^n(x_i-\bar{x}_i)^2 - \sum_1^n(x_i-\hat{x}_i)^2}{\sum_1^n(x_i-\bar{x}_i)^2} \quad (3)$$

$$173 \quad APD = \frac{1}{N} \sum_{i=1}^N |x_j - x_i| / x_i \quad (4)$$

174 Where the x_j is the SPM retrieved by algorithm, the x_i is the in-situ SPM, and the \hat{x}_i is the value of in-situ SPM
 175 regression fit, and the \bar{x}_i is the mean value of in-situ SPM.

176 2.4.3 Establishment and validation of the retrieval algorithm.

177 Table. 1 showed single band algorithms with three common empirical function type, and the index form in
 178 near infrared (NIR) band is the best selection with R^2 0.91 and APD 34.88%. Moreover, the composition, size and
 179 shape of the particles are extremely complex in high turbid waters (with the concentration up to 2000mg/L) like the

180 YRE (He et al., 2013). Single-band algorithms are susceptible to interference from above environmental conditions,
 181 so it is difficult to fully reflect the spectral information of different SPM. Band ratio could weaken or even
 182 eliminate the effects of particle size and light to a certain extent (Doxaran et al., 2002). Some representative band
 183 ratio algorithms using various function type were listed in Table. 2, and the optimal algorithm is marked. Fig. 5 is
 184 the scatter plot of in-situ SPM against estimates from the optimal SPM algorithm in the YRE. The in-situ and
 185 estimated SPM were distributed along the 1:1 line, and it showed a good relationship between in-situ and estimated
 186 SPM values in the YRE with an APD of 33.12% and R² of 0.93.

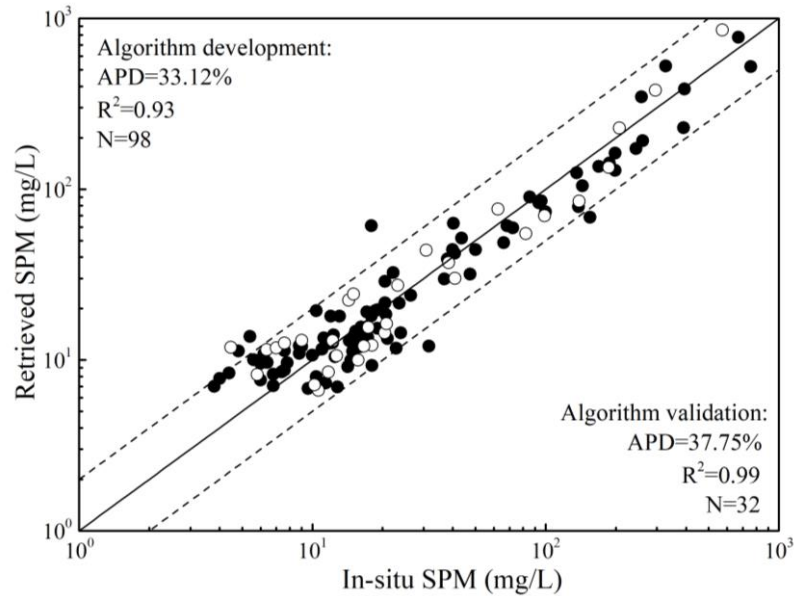
187 Table. 1 Retrieval algorithms in the YRE with single band

Sensor	Function type	a	b	c	R ²	APD (%)
OLI	Lg SPM=aR _{rs} 561 ^b	37.391	0.944	/	0.60	89.96
	Lg SPM=aR _{rs} 655 ^b	10.564	0.531	/	0.79	67.14
	Lg SPM=aR _{rs} 865 ^b	6.644	0.265	/	0.91	34.88
	Lg SPM=ae ^{bR_{rs}561}	0.553	28.374	/	0.66	84.52
	Lg SPM=ae ^{bR_{rs}655}	0.667	24.625	/	0.81	55.80
	Lg SPM=ae ^{bR_{rs}865}	1.251	18.614	/	0.65	83.39
	Lg SPM=aR _{rs} 561 ² +bR _{rs} 561+c	829.368	13.593	0.918	0.66	83.85
	Lg SPM=aR _{rs} 655 ² +bR _{rs} 655+c	255.252	12.731	0.837	0.88	42.76
	Lg SPM=aR _{rs} 865 ² +bR _{rs} 865+c	-940.423	92.117	0.989	0.90	39.65

188 Table. 2 Band ratio retrieval algorithms with fitting coefficient in the YRE

Function Form	R ²	APD (%)
Lg SPM=0.489+ 24.765R _{rs} 865+0.758R _{rs} 655/R _{rs} 561	0.92	34.33
Lg SPM=0.786+17.061R_{rs}655+1.316R_{rs}865/ R_{rs}561	0.93	33.12
Lg SPM=0.793+17.052R _{rs} 655+0.758R _{rs} 865/R _{rs} 482	0.93	33.69
Lg SPM=0.530+1.501R _{rs} 865/R _{rs} 561+0.930R _{rs} 655/R _{rs} 561	0.93	59.40
Lg SPM=3.099(R _{rs} 865/ R _{rs} 561) ^{0.329}	0.91	34.84
Lg SPM= 2.032(R _{rs} 655/ R _{rs} 561) ^{2.582}	0.86	41.69
Lg SPM=1.176e ^{1.125(R_{rs}865/ R_{rs}561)}	0.75	69.12
Lg SPM=0.546e ^{1.224(R_{rs}655/ R_{rs}561)}	0.88	38.68
Lg SPM=-2.209(R _{rs} 655/R _{rs} 561) ² +4.418(R _{rs} 655/R _{rs} 561) +0.908	0.90	38.74
Lg SPM=1.043+2.55(R _{rs} 655/ R _{rs} 561)	0.84	49.56

189



190

191

Fig. 5. The scatter plot with the optimal algorithm by Landsat 8 OLI. The solid dots are used to create

192

algorithm, and the hollow dots are used to test the algorithm.

193

3. Result

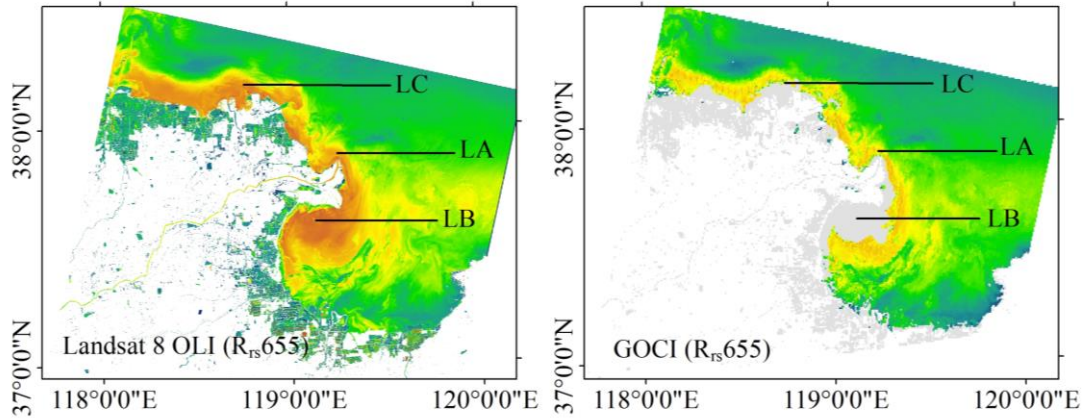
194

3.1 Landsat 8 OLI measured R_{rs} compared to GOCI measurements

195

Due to the low temporal resolution (16 days) of Landsat 8 and frequent cloud coverage in the YRE, it is difficult to identify a matched observation between satellite and in-situ data. Therefore, it is not reasonable to validate Landsat 8 OLI measured R_{rs} directly using in-situ observation. GOCI is the world's first geostationary satellite successfully launched in June 2010 which has the coverage of 2500×2500 km square (Choi et al., 2012). Due to its high temporal resolution (eight images per day with one-hour intervals.), GOCI has been widely used to estimating the concentration of surface suspended matter in seawater in recent years (Choi et al., 2014; He et al., 2013). Li et al. (2016) evaluated the stability of the GOCI-derived ocean color remote sensing products under different observing time, and the result showed that the R_{rs} retrieved by KOSC algorithm has the best agreement with the values of in-situ observations in Liaodong Bay. Sun et al. (2020) confirmed the accuracy of GOCI R_{rs} by analyzing the change of the surface suspension concentration in the Bohai Bay in winter. These all prove that R_{rs} of GOCI with high accuracy, and as a result, the study proposed a validation of Landsat 8 OLI R_{rs} based on cross validation with GOCI measurement. The GOCI L1B data were got from KOSC (http://kosc.kiost.ac.kr/eng/p10/kosc_p11.html), and the L1B products were processed by a series of procedures including Rayleigh scattering, aerosol scattering and genuine seawater reflectance integrated in GDPS of KOSC (Gordon et al., 1988; Wang, 2005; Wang & Gordon, 1994).

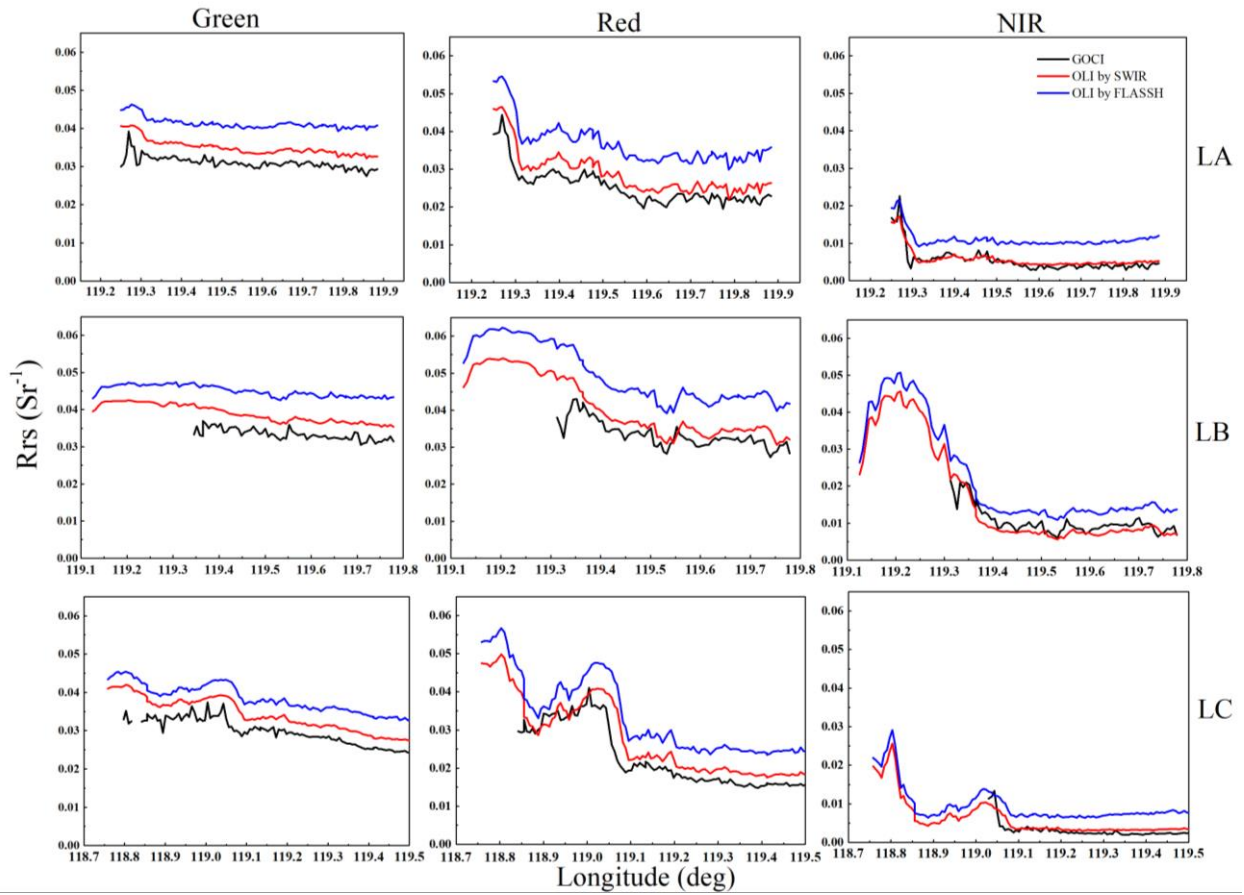
209



210
 211 Fig. 6. Landsat 8 OLI $R_{rs}(655)$ versus GOCI $R_{rs}(660)$. Gray areas denoted mask areas. Three transects (marked as
 212 LA, LB and LC) in the figure were used for the cross validation of Landsat 8 OLI measured R_{rs} and GOCI
 213 measurements.

214 In addition to using the SWIR method for atmospheric correction, this study also used the FLAASH method to
 215 perform atmospheric correction on Landsat 8 OLI data. Two R_{rs} result about Landsat 8 OLI (SWIR and FLAASH)
 216 were compared to R_{rs} (GOCI) result, and the cross validation were performed along west-east transects shown in
 217 Fig. 6. Larger areas with no useful data were obtained for GOCI $R_{rs}(660)$ due to the atmospheric overcorrection.
 218 The cross-validation results were shown in Fig. 7. Although band setting of two sensors were slightly different, Fig.
 219 7 showed excellent matched comparisons of R_{rs} . It's notable that R_{rs} from FLAASH atmospheric correction were
 220 significantly higher than those of SWIR atmospheric and GOCI. Therefore, it is not a good choice to retrieve R_{rs} by
 221 FLAASH method in this study area. For SWIR method, the two R_{rs} from the two sensors have good consistency
 222 especially in red and NIR band. The R_{rs} behaved consistency with decreases from west to east. A relatively large
 223 difference was observed in modestly turbid regions. The value of R_{rs} in red and NIR band was high in turbid regions,
 224 but in the other modestly and low turbid regions, R_{rs} mostly at low level with its value below $0.03 S_r^{-1}$.

225 Fig. 8 shows the R_{rs} of central wavelength derived from Landsat 8 OLI (SWIR) and GOCI, and table 3 shows
 226 the APD between the two sensors. The R_{rs} distribution derived from the two sensors are consistent. The difference
 227 between Landsat 8 and GOCI reduced with the wavelength increased. Relatively high R_{rs} were found at the mouth
 228 of the Yellow River, north of Bohai Bay and the west of Laizhou Bay. Although the distribution of the two R_{rs} were
 229 similar, higher R_{rs} were obtained from Landsat 8 OLI. All APD fell within a range less than 15%, and the smallest
 230 was observed in NIR bands with its mean APD 13.56%.



231

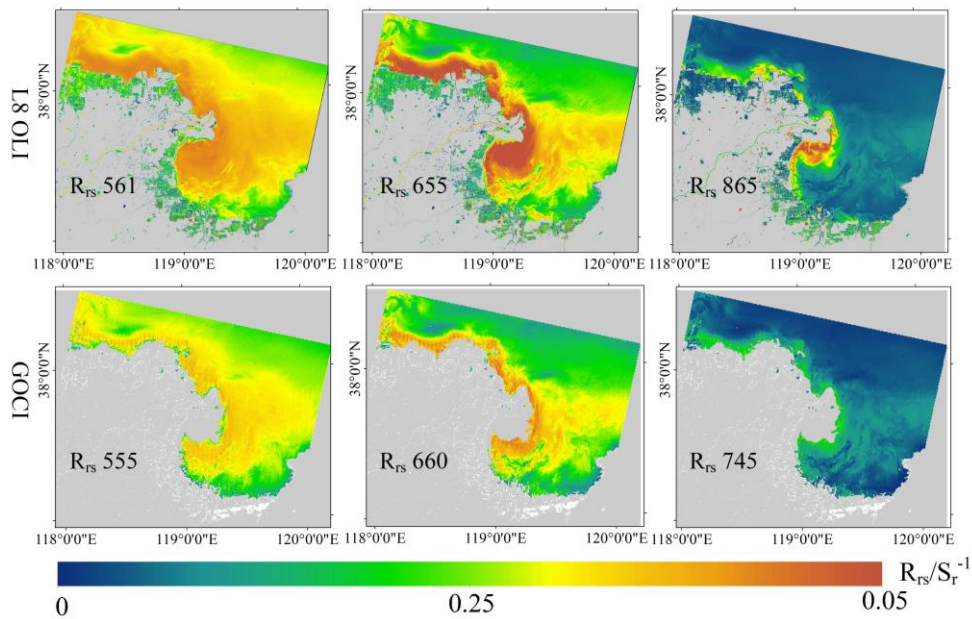
232

233

234

235

Fig. 7. Comparisons of measured R_{rs} between Landsat 8 OLI and GOCI along three west-east transects. Three bands from left to right: Green [Landsat 8 OLI $R_{rs}(561)$ versus GOCI $R_{rs}(555)$]; Red [Landsat 8 OLI $R_{rs}(655)$ versus GOCI $R_{rs}(660)$]; NIR [Landsat 8 OLI $R_{rs}(865)$ versus GOCI $R_{rs}(745)$]. And three transects from left to right: transects LA, LB, and LC.



236

237

238

Fig. 8. Comparisons of the retrieved R_{rs} between the Landsat 8 OLI and GOCI on 26 August, 2016 (The Landsat 8 OLI image was obtained at UTC 2:42, and the GOCI image was obtained at UTC 2:28).

Table. 3. The APD (%) of R_{rs} between Landsat 8 (SWIR) and GOCI in three lines.

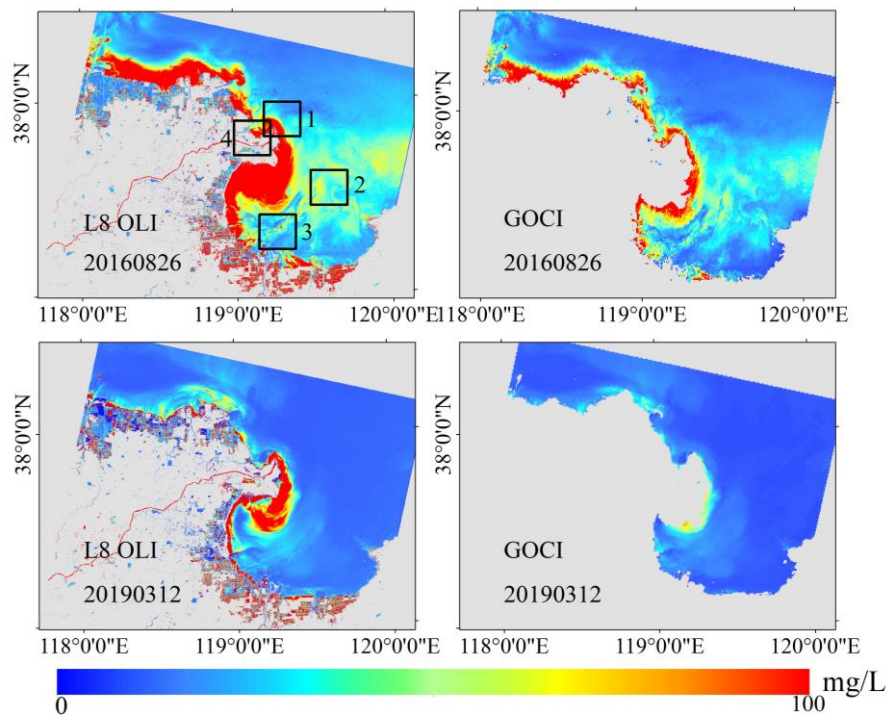
	Green	Red	NIR
LA	13.66	13.50	13.38
LB	14.15	13.63	13.88
LC	15.80	14.48	13.43
Mean (LA, LB, LC)	14.54	13.87	13.56

240 3.2 Mapping SPM using Landsat 8 OLI and GOCI

241 Some previous studies mapped the diurnal dynamics of SPM in turbid coastal waters using GOCI, along with
 242 numerous empirical algorithms for SPM have been developed in various estuaries and coasts (Choi et al., 2013; He
 243 et al., 2013; Ruddick et al., 2012). The study compared the result of the retrieved SPM between Landsat 8 OLI and
 244 GOCI, and two high-quality images on the same transit date (26 August 2016 and 12 March 2019). In order to
 245 compare the retrieval result, the same retrieval model including similar bands selection and function form was
 246 applied to GOCI, and the algorithm was described in Eq (5). Fig. 9 showed spatial distribution of SPM retrieved
 247 from Landsat 8 OLI and GOCI, and the spatial distribution of Landsat 8 OLI is generally consistent with that of
 248 GOCI. Furthermore, in order to quantify the SPM result, the SPM value were extracted from LA, LB and LC in two
 249 days, and the SPM result from two sensors were showed in Fig. 10. The SPM value from two sensors were similar
 250 with APD no more than 40%, but the SPM value from Landsat 8 OLI are slightly higher than that of GOCI, which
 251 is consistent with the previous result (Pan et al., 2018).

$$252 \quad Lg \text{ SPM} = 0.82389 + 13.18944R_{rs}(680) + 1.15577R_{rs}(745)/R_{rs}(555) \quad \text{Eq (5)}$$

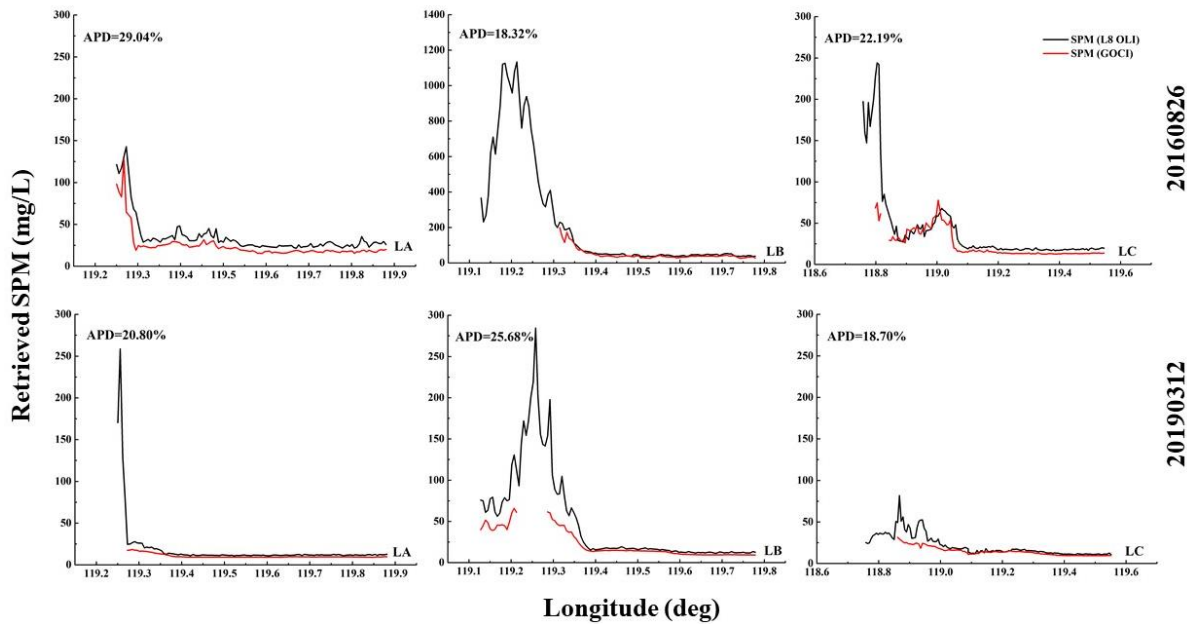
253 Where the R_{rs} represent the remote sensing reflectance of different bands from GOCI.



254

255

Fig. 9. Comparison of the estimated SPM from Landsat 8 OLI to GOCI on 26 August 2016 and 12 March 2019.



20160826

20190312

256

257

258

259

260

261

262

263

264

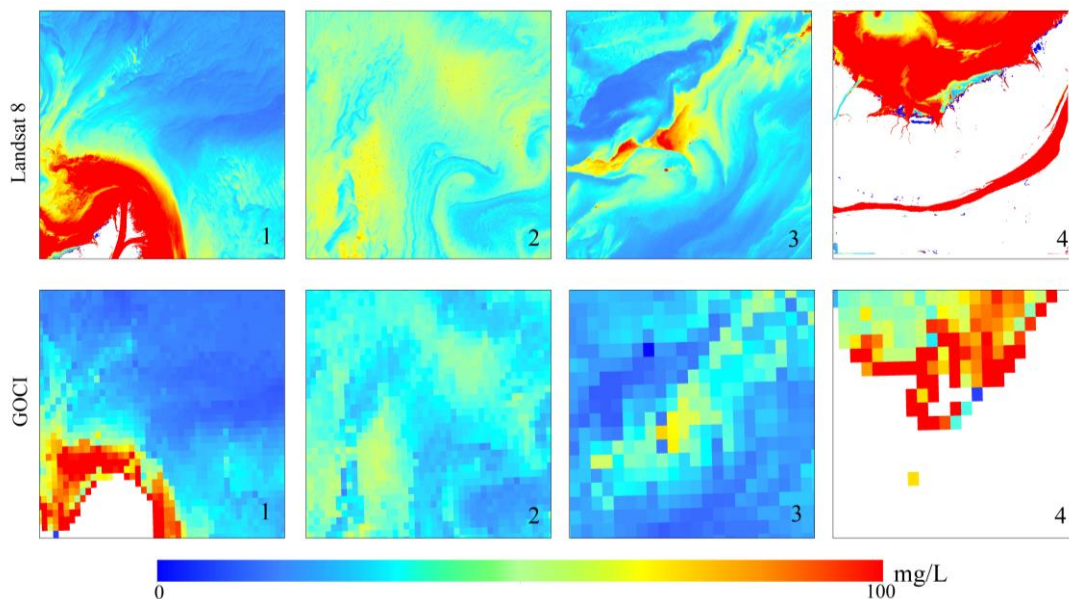
265

266

267

Fig. 10. Comparisons between Landsat 8 OLI and GOCI derived SPM along west-east transects, and APD is the relative error between the two sensors.

Fig. 11 showed the details of the distribution of SPM from Landsat 8 OLI and GOCI respectively. Clearly, the SPM from OLI image with a 30m spatial resolution shows more details about the spatial distribution of the SPM within and outside the estuary of the Yellow River. Fig.11 show the details of comparisons of distribution about SPM in the black boxes numbered 1-4 in Fig. 9. The distribution of SPM in OLI images were much clearer than that in GOCI. In addition, the yellow river main road is clearly observed in the OLI image, but its not appeared in GOCI image. SPM distribution trend and flow direction were also obviously shown in OLI images. The difference of SPM distribution near the YRE clearly demonstrates the effects of the river discharge on the spatial distribution of the SPM. The above results show that Landsat 8 OLI is superior to GOCI in clearly observing the SPM spatial distribution.



268

269

270

Fig. 11. The details of SPM spatial distribution in four selected typical locations between Landsat 8 OLI and GOCI. The first row are the SPM distribution of Landsat 8 OLI, and the second row are GOCI.

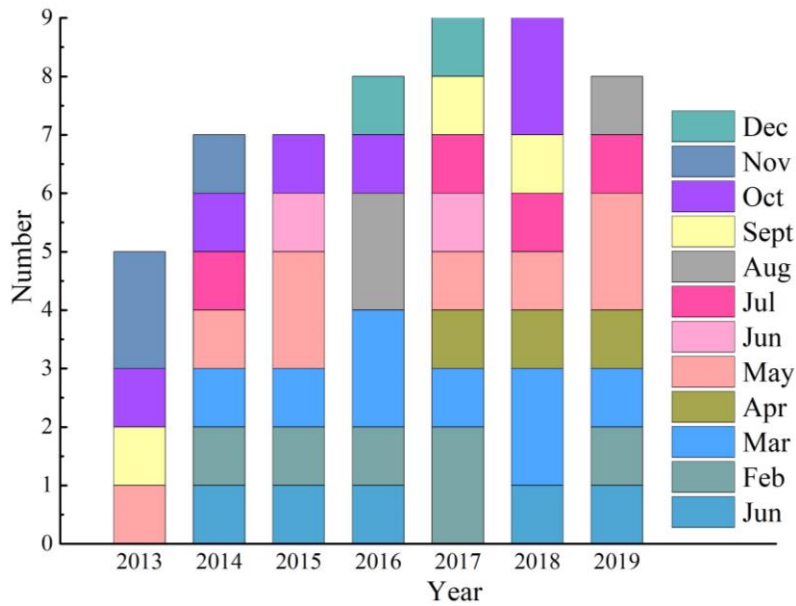
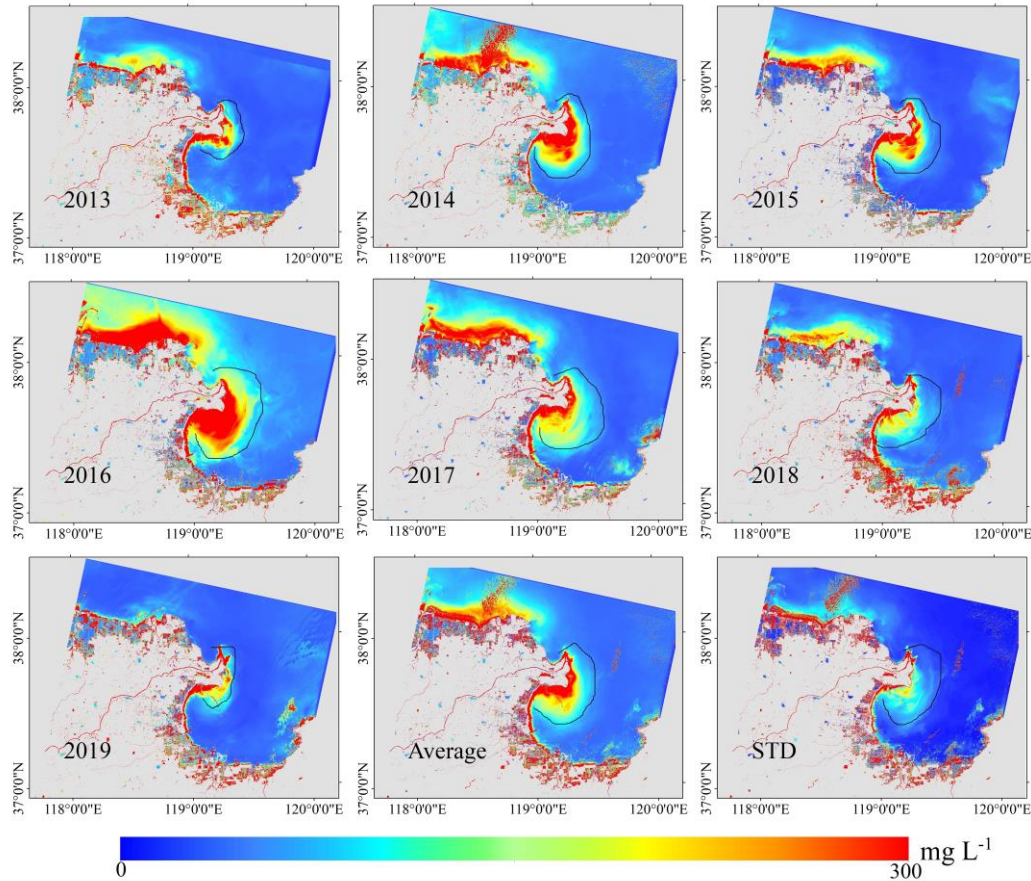


Fig. 12. Images quantity of this study in different months from 2013 to 2019.

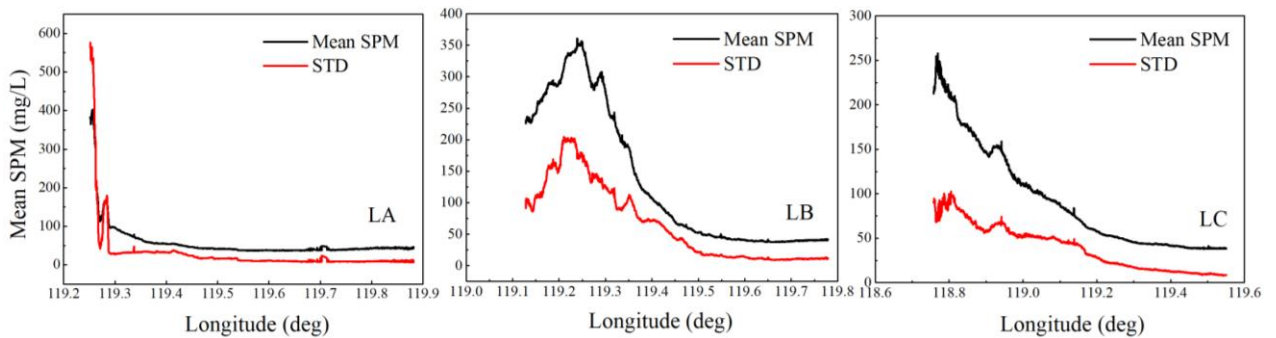
Fig. 12 shows the number of used images in different month during 2013 to 2019, and the number of images was evenly distributed. Fig. 13 shows the annual mean SPM distribution in the YRE, the average SPM distribution and standard deviation (STD) over the 7 years, which was retrieved from Landsat 8 OLI in the YRE. SPM presents ovate distribution near the Yellow River mouth marked by the black coils in Fig. 13. The mean SPM in the YRE is generally increasing from 2013 to 2016, while decreasing from 2016 to 2019, and it maybe because the variation of annual total sediment discharge from Yellow River. Significantly high SPM was found in the Yellow River mouth, northwestern parts of the Laizhou Bay, south part of the Bohai Bay with its SPM even more than 10^3 mg/L. SPM decreased from Yellow River mouth to the east, and relatively low SPM were also found south and east of the Laizhou Bay with the smallest value in the order of 10mg/L. SPM near the Yellow River mouth and adjacent areas were approximately two to three orders higher than those for other regions, demonstrating that most SPM quickly subsided near the estuary.

Fig 13 also showed STD and average of SPM distribution over all 53 images. Spatial distribution of STD were similar to that of mean SPM, which was consistent with the previous conclusion (Qiu et al., 2017). In the low concentration area, STD of all 53 images normally fell within a range of 5mg/L to 10mg/L, while 10–50 mg/L in the higher concentration region. The variation of SPM concentration is minimal in the low concentration areas over 7 years. Enhanced variations can be found near the Yellow River mouth, northwest part of the Laizhou Bay and south part of Bohai bay with the STD more than 100mg/L. The high SPM concentration and the variability is primarily due to the sediment discharge, and also possibly due to the wind-driven resuspension of the bottom sediment for the shallow water. Quantifying mean SPM and STD by the three west-east transects, and the result showed in Fig.14. The STD of SPM were all about 10mg/L in the east of study area, which indicated SPM in the east of study area has no visible difference in all 7 years. In contrast, the STD changed a lot in high turbid areas like Yellow River mouth and its adjacent areas with its value more than 100mg/L. In addition, Fig. 13 shows that highly varying SPM distributions were consistent with high concentration SPM and vice versa. This also appeared in comparisons between mean SPM and STD along the three west-east transects in Fig. 14.



298
299
300

Fig. 13. Distribution of the mean annual SPM and Seven-year average standard deviation retrieved by Landsat 8 OLI from 2013 to 2019.



301
302
303
304

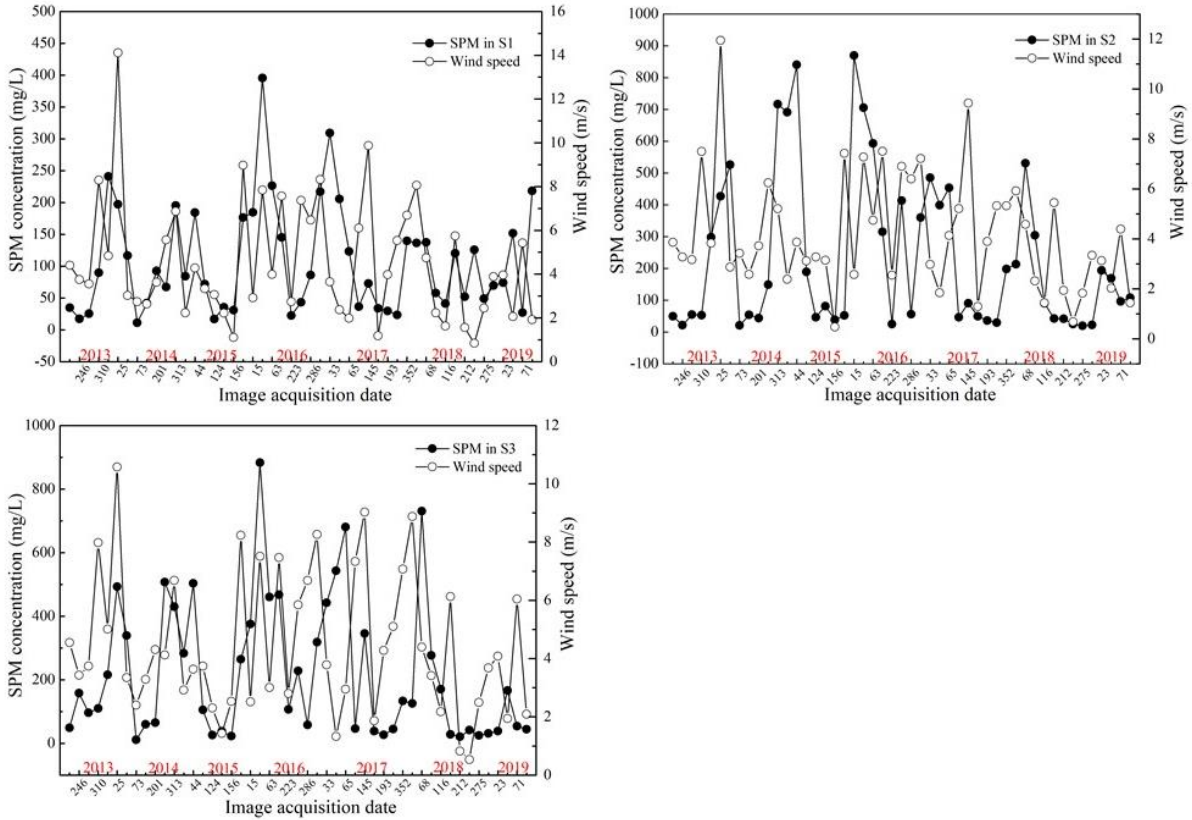
Fig. 14. Comparisons between mean SPM and standard deviation (STD) along the three west-east transects in three different lines (shown in Fig. 6). Mean SPM and STD were derived from 2013 to 2019 Landsat8 OLI retrieved.

305 4. Discussion

306 4.1 The effect of wind speed on distribution of SPM.

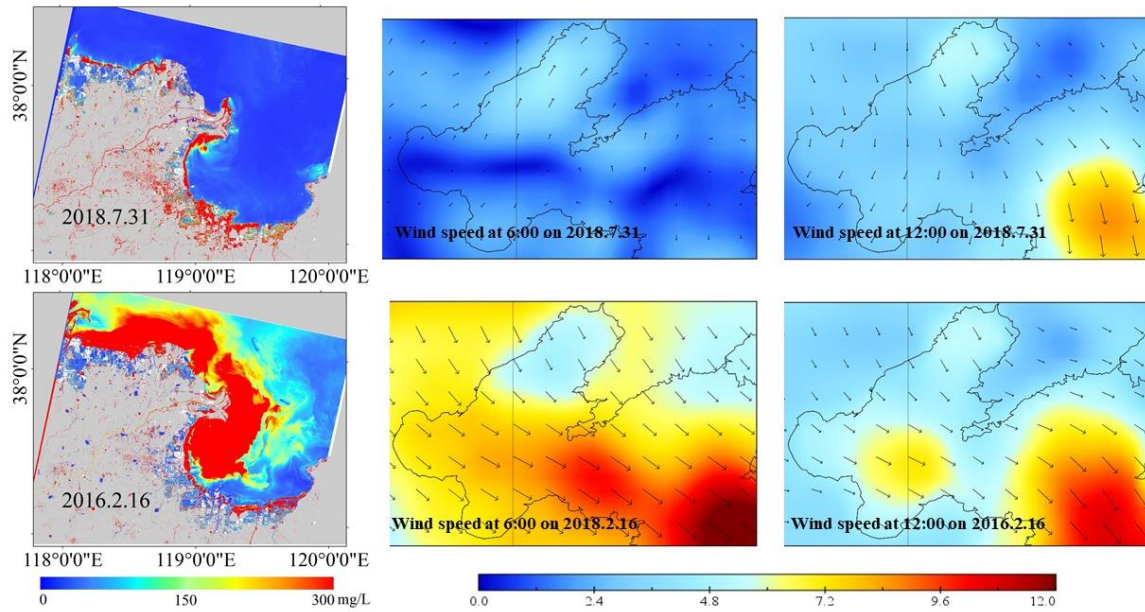
307 Many previous studies have shown that wind was an important factor on SPM (Booth et al., 2000; He et al.,
308 2013; Qing et al., 2014). Wind controls the deposition and resuspension of sediment from Yellow River and seabed
309 (Wiseman et al., 1986). He et al. (2013) reported that the SPM and its diurnal variation increased under the
310 influence of Typhoon Meari. In order to further quantify the SPM seasonal variation and give an explanation about
311 the impact mechanism of strong wind on the changes in SPM. The study selected three representative pixel boxes

312 S1, S2, and S3 (40×40 pixels) which were located near the Yellow River mouth, the north of Laizhou Bay and the
 313 south of the Bohai Sea, respectively (the location of three boxes were showed in Fig. 1). Fig. 15 showed the
 314 relationship between SPM and wind speed. The wind speed data were from the Cross-Calibrated Multi-Platform
 315 (CCMP) (<http://www.remss.com/measurements/ccmp/>). The SPM changed with wind speed, and high wind speed
 316 corresponded to high SPM which fully explained the impact of wind speed on the variation of SPM.



317
 318 Fig. 15. The relationship between SPM and wind speed in the three representative areas (S1, S2, S3). The
 319 x-axis represents the number of days in the year.

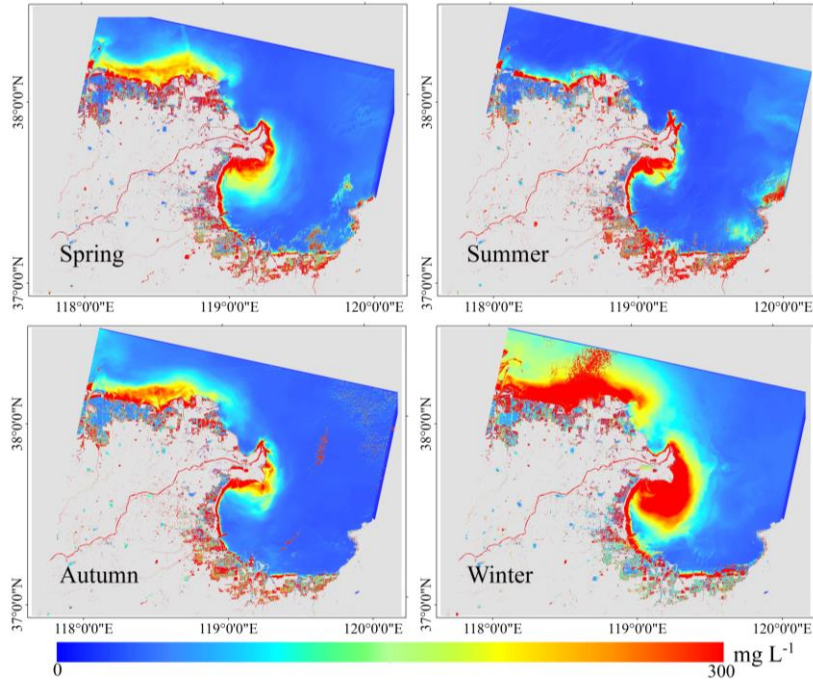
320 Fig. 16 compared SPM distribution in two days, and the wind condition in the two days were different. Higher
 321 SPM and wider ranges of SPM distribution were observed on 16 February 2016, and in which day, wind speed is
 322 between 4.8m/s to 8.4m/s in the study area. (The wind speed were drawn from CCMP at 10m from sea surface and
 323 the obtained time was 6:00 and 12:00). In contrast, a maximum wind speed only reached 4.6m/s on 31 July 2018.
 324 The distribution of SPM has big difference in the two days. SPM reached and even larger than 300mg/L under
 325 strong wind, and the SPM was about 10mg/L to 50mg/L under a weak wind condition. High SPM corresponds to
 326 heavy wind which further effectively confirmed wind speed is a major force that controls the SPM variation.



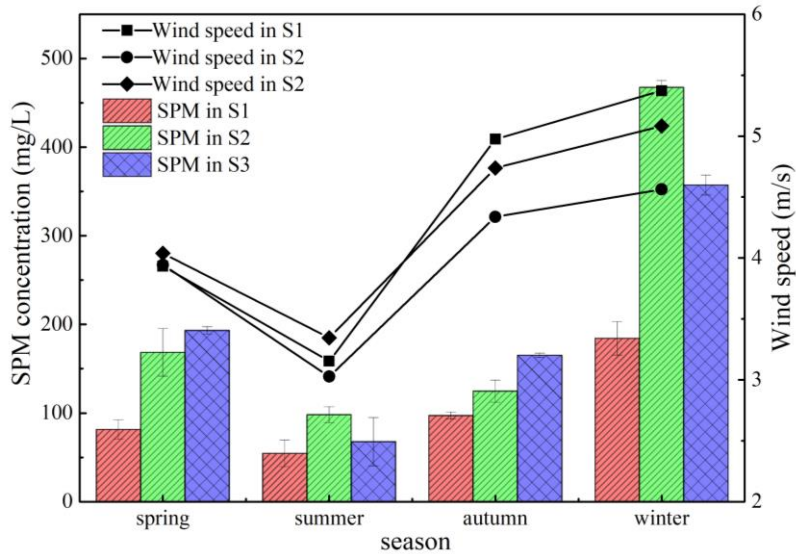
327

328 Fig. 16. SPM distributions mapped by Landsat 8 OLI under different wind conditions. The images were
 329 acquired on 20160216 (Three images of the first row) with maximum wind speed 4.6m/s and on 20180731 (Three
 330 images of second row) with maximum wind speed 8.4m/s.

331 The wind field of Bohai Sea exists obvious seasonal characteristic, and the storm wave was strong in winter
 332 but weak in summer. Bohai Sea prevailing north wind in winter with wind speed was about more than 17m/s, while
 333 prevailing wind of summer was southeasterly with wind speed between 4m/s to 6m/s (Yu et al., 2013). Strong wind
 334 pattern frequently constitutes a major force that controls the deposition and resuspension of riverborne sediments in
 335 the YRE (Wiseman et al., 1986). Based on the impact of wind on SPM variation, the SPM also presented similar
 336 seasonality with wind storm. Fig. 17 shows the seasonal mean SPM distribution in the YRE, and numbers of
 337 Landsat 8 OLI images in spring (March, April and May), summer (June, July and August), autumn (September,
 338 October and November) and winter (December, January and February) were 19, 9, 12 and 13. SPM showed strong
 339 seasonality, being high in winter and low in summer like wind variation pattern. Fig. 18 showed the seasonal SPM
 340 concentration and wind speed in three representative boxes, and the result indicate that SPM and wind with the
 341 same variation pattern in difference season. SPM concentration at the highest level in winter with average SPM
 342 about 300mg/L, and at the same time , strong wind appeared in winter.

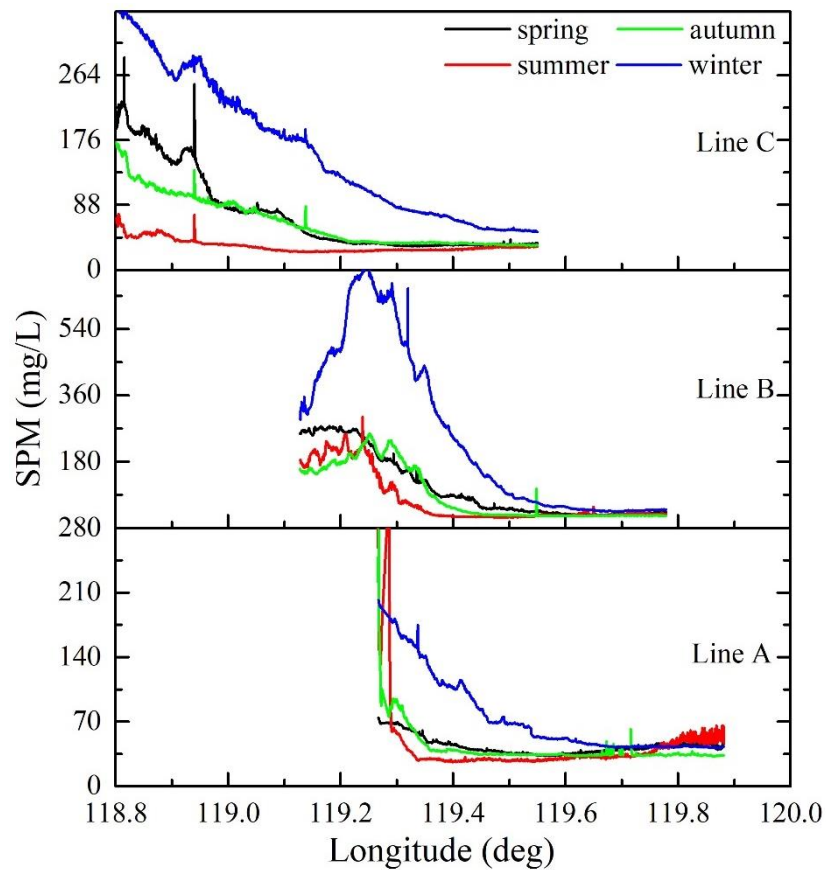


343
344 Fig. 17. The mean seasonal SPM retrieved by Landsat 8 OLI from 2013 to 2019 and red range demark the the
345 maxima concentration zone.



346
347 Fig. 18 The variation of SPM concentration and wind speed with season.

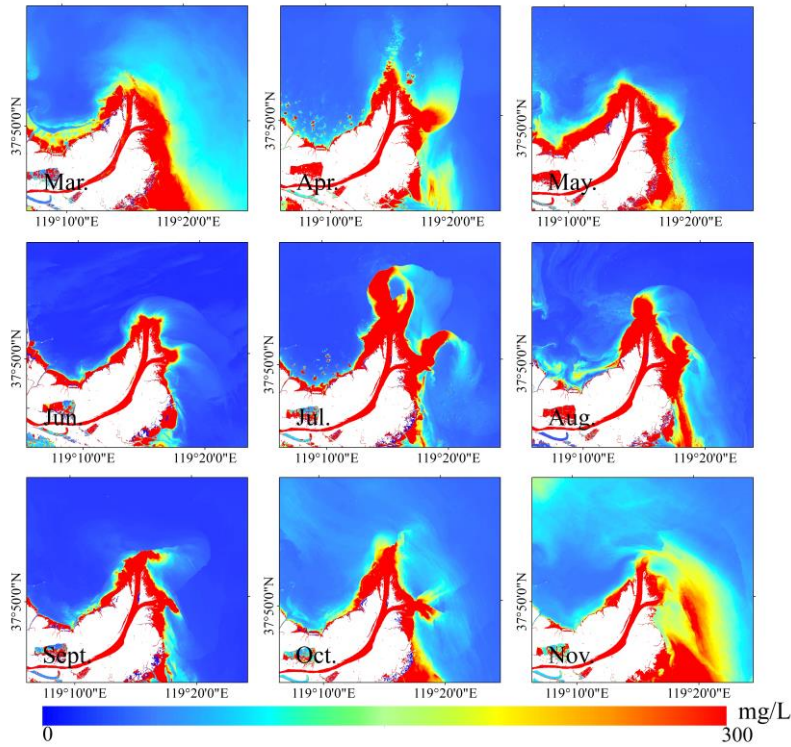
348 Fig. 19 showed the value of seasonal SPM variations along three west-east transects to further quantified SPM
349 seasonal variation. It's noted that SPM in Line "A", "B" and "C" follow the same variation pattern, but the
350 difference of SPM concentration value in different seasons. SPM generally decreased from west to east the study
351 areas which are consist with the result of annual average distribution of SPM. The mean SPM distribution have
352 significant difference between four seasons in turbid regions near the yellow river mouth. In contrast, little seasonal
353 variation in the distribution of SPM in the areas of low SPM concentration like the east of study area. SPM
354 concentration in spring and autumn performs similar pattern and magnitude. SPM in winter was much higher than
355 other seasons with maximum SPM reaching about 500mg/L. While SPM in summer were all at the lowest level
356 with SPM all less than 100mg/L except a small part of turbid areas. The monsoon climate affected the seasonal
357 variability of SPM and distribution more notably, and strong wind drive tall waves resulting in high SPM in winter



359
 360 Fig. 19. Comparisons between mean seasonal SPM along the three west-east transects (LA, LB and LC were shown
 361 in Fig. 6). Mean seasonal SPM were derived from 2013 to 2019 Landsat 8 OLI measurements.

362 4.2 The effect of river discharge on distribution of SPM.

363 In addition to wind speed, SPM is effected by numerous factors such as tidal, river discharge, and previous
 364 studies have shown that the river discharge was the main factor in fluid dynamics in estuary area (Bailey & Werdell,
 365 2006; Li et al., 2019; Liu et al., 2013; Pan et al., 2018; Shi & Wang, 2012; Su & Wang, 1989; Zhang et al., 2014).
 366 The river discharge was large from May through October, and the value was low from November to April. Yellow
 367 river had an unique Water-sediment Modulation through Xiaolangdi dam since 2002 which resulted in abnormal
 368 higher runoff in July (Qiu et al., 2017). River discharge in wet season were obviously higher than that in dry season.
 369 River runoff increased first and then decreased from May to October, and maximum value about 1600m³/s
 370 appeared in July. A relatively low level of the river runoff displayed in dry season (from November to April), and
 371 the value were all about 300 m³/s. In general, SPM in the YRE inputted by the yellow river are much higher in wet
 372 seasons than that in dry seasons (Qiu et al., 2017). Li et al. (2019) suggested that SPM in wet season were higher
 373 than that in dry season in the 3km buffer area of the Yellow River mouth, and SPM were similar as the water
 374 discharge load at Lijin Hydrological Station which loacted 100km away from yellow river mouth.



375

376 Fig. 20. Monthly mean SPM maps in yellow river mouth area retrieved by Landsat 8 OLI in the YRE from 2013 to
 377 2019.

378 Yellow River carries a large amount of sediments annually into the Yellow River mouth and its adjacent areas
 379 waters. The study analyzed the influence of river runoff on SPM variation at monthly scale. Section 4.1 showed that
 380 strong wind resulted in highly SPM through resuspend sediment, and in order to excluded the effect of wind, the data
 381 with strong wind (Jan, Feb and Dec) were removed. Fig. 20 shows the monthly average distribution of SPM from
 382 2013 to 2019 in the YRE, and monthly satellite-derived SPM distribution in the study area presented a high
 383 seasonal variability which was consistent with the previous studies (He et al., 2013; Li et al., 2019; Qiu et al., 2017).
 384 SPM in the yellow river mouth gradually increasing from June to the maximum in July and August and then
 385 decreased after September, which is closely correlated with yellow river discharge. Higher SPM concentrated near
 386 the estuary and presented variation of different magnitudes and extents. Yellow River mouth area had a relatively
 387 high SPM in the wet season (from May to October) compared with that in the dry season (from November to
 388 April). High concentration SPM still appeared at a farther distance from YRE in wet season compared to dry
 389 season, which was primarily due to river discharge.



Fig. 21. The location of buffers along the Yellow River direction.

390

391

392

393

394

395

396

397

398

399

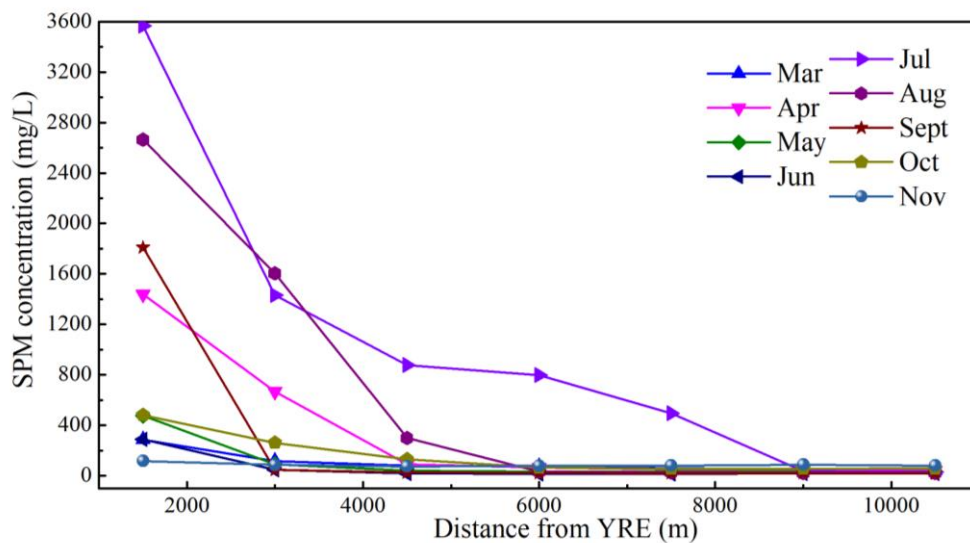
400

401

402

403

In order to further quantitative explore the relationship between river discharge and SPM concentration, the study set up 7 buffer zones along the straight line direction of yellow river runoff. The buffers were set to select 50 × 50 pixels per 1.5 km to study scope of the influence of river discharge, and the center position of the pixels of buffers were shown in Fig. 21. SPM in July and August were higher than other months with maximum concentrations more than 3000mg/L, while the concentration was relatively low in dry season such as November and March with maximum concentration only less than 500mg/L. SPM gradually decreased with the distance increased from yellow river mouth, but the degree of decline in SPM presented obvious monthly difference. SPM changed with the distance increased relative obviously when the buffer distance less than 4.5km, while the distance increased the variation of SPM was no longer obvious. The extent affected by yellow river discharge was more near the yellow river mouth which indicated that the discharged sediment was trapped in inshore waters and cannot directly influence the distribution of SPM out of the estuary. However, the SPM were still at high level within 8km zones in July which were consistent with the high level river runoff in the two months as Fig. 22 shows.



404

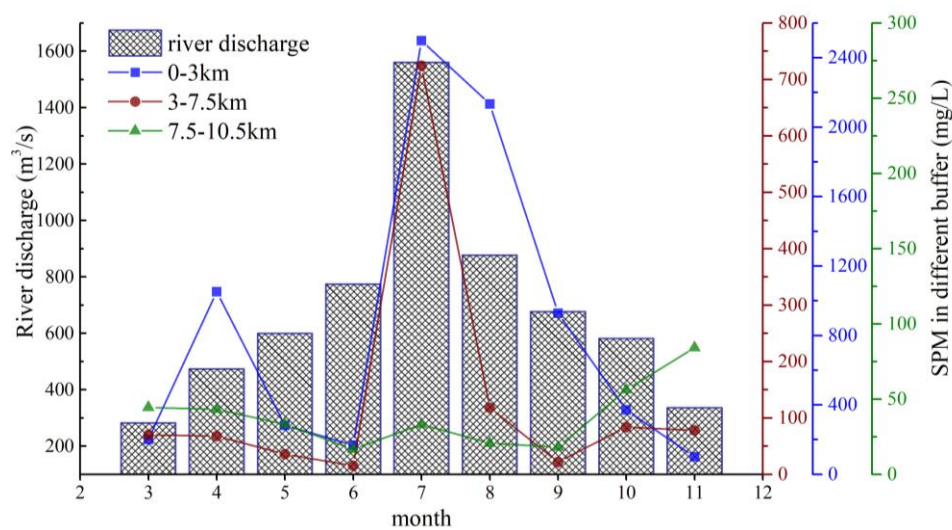
405

406

Fig. 22. The variation of SPM with the distance from YRE in 12 months.

The study redistributed 7 buffers according to the trend of SPM, and the new three buffers were 0km to 3km,

407 3km to 7.5km and beyond 7.5km. Fig. 23 was the monthly mean river discharge and monthly mean SPM from
 408 2013 to 2019 under new buffers. The trend of SPM was consistent with river runoff, which further indicated that
 409 the river discharge was the main factor on SPM distribution near the yellow river mouth. SPM at high level with
 410 maximum more than 2400mg/L and minimum about 100mg/L within the first buffer (0-3km), and affected by large
 411 river runoff, SPM in July and August were much higher than others. Although the consistency between SPM and
 412 river discharge also exist in the second buffer (3-7.5km), SPM concentration was much smaller than the first with
 413 maximum value about 750mg/L and minimum about less than 50mg/L. In contrast, SPM no longer change with the
 414 river runoff in the last buffer (beyond 7.5km), and the maximum concentration no longer appeared in wet season. In
 415 addition, SPM was quite low with concentration value between 0mg/L to 150mg/L at farther offshore. The above
 416 result indicated that the influence of river discharge on SPM was limited, and when the distance from YRE was
 417 far-off, the river discharge no longer affected the SPM changement. However, within the threshold range, SPM
 418 change with the river runoff and the trends of SPM and river discharge were consistent. This conclusion was
 419 consistant with the result in ChangJiang estuary ([Shang & Xu, 2018](#)).



420
 421 Fig. 23. The monthly mean river discharge and the SPM in three redistributed buffers from 2013 to 2019. Please
 422 note the consistency of the SPM coordinate colors.

423 5. Conclusions

424 This study assessed the capability of Landsat 8 OLI to estimate SPM concentration in the YRE and then
 425 monitor the dynamics of SPM in this complex environment. Multiyear and seasonal mean distribution of SPM and
 426 related variation were derived from Landsat 8 OLI data from 2013 to 2019. Landsat 8 OLI measured R_{rs} was
 427 cross-validated with GOCI measurements, which were proved good R_{rs} product by others. The validation showed
 428 that the Landsat 8 OLI can generate reasonably good R_{rs} by SWIR atmospheric correction method. This study
 429 proved that red and NIR reflectance data from Landsat 8 OLI are well suited to retrieve SPM by analyzing SPM in
 430 different concentration ranges, and the Pearson correlation coefficient between SPM. An optimal algorithm was
 431 established with an APD 33.12% and high R^2 0.93 to estimate SPM concentration and distribution. The results
 432 supported SPM inversion and it were proved good algorithms to retrieve SPM in Yellow River Estuary.

433 It's well known that the YRE with high SPM, but the mean annual and seasonal maps show that highly turbid
 434 water is most found in an ovate surrounding the mouth of the yellow river. High SPM was also in northwestern part
 435 of Laizhou Bay and south part of Bohai Bay with SPM even more than 10^3 mg/L. High SPM variations are
 436 consistent with high SPM and vice versa. Significant difference was found in different seasons. Higher SPM in
 437 range and intensity were found in the dry season like winter than in the wet season like summer.

438 The SPM distribution in the YRE were affected by river discharge and strong wind. Higher SPM

439 concentration near the yellow river mouth from June to August is closely correlated with yellow river runoff, but
440 this impact is limited due to the distance. When the distance from the YRE more than 4.5km, the impact of river
441 discharge is no longer significant. Strong wind increased SPM in the YRE and its adjacent areas. However, the
442 effect of strong winds was unsustainable which was affected by seasonal climate. Significant seasonal SPM
443 variations are mainly controlled by sediment resuspension processes driven by wind-wave forces.

444 Landsat 8 OLI as a land satellite, and its targets is to monitor land. This study showed that Landsat 8 OLI data
445 can also be applied to quantify SPM distribution and variation of SPM in the Yellow River estuary.

446 Reference

- 447 Bailey, S. W., & Werdell, P. J. (2006). A multi-sensor approach for the on-orbit validation of ocean color satellite data
448 products. *Remote Sensing of Environment*, 102(1-2), 12-23. doi:<https://doi.org/10.1016/j.rse.2006.01.015>
- 449 Binding, C. E., Bowers, D. G., & Mitchelson-Jacob, E. G. (2005). Estimating suspended sediment concentrations from
450 ocean colour measurements in moderately turbid waters; the impact of variable particle scattering properties.
451 *Remote Sensing of Environment*, 94(3), 373-383. doi:<https://doi.org/10.1016/j.rse.2004.11.002>
- 452 Booth, J. G., Miller, R. L., McKee, B. A., & Leathers, R. A. (2000). Wind-induced bottom sediment resuspension in a
453 microtidal coastal environment. *Continental Shelf Research*, 20(7), 785-806.
454 doi:[https://doi.org/10.1016/S0278-4343\(00\)00002-9](https://doi.org/10.1016/S0278-4343(00)00002-9)
- 455 Choi, J.-K., Park, Y. J., Ahn, J. H., Lim, H.-S., Eom, J., & Ryu, J.-H. (2012). GOCI, the world's first geostationary ocean
456 color observation satellite, for the monitoring of temporal variability in coastal water turbidity. *Journal of*
457 *Geophysical Research: Oceans*, 117(C9). doi:<https://doi.org/10.1029/2012JC008046>
- 458 Choi, J.-K., Park, Y. J., Lee, B. R., Eom, J., Moon, J.-E., & Ryu, J.-H. (2014). Application of the geostationary ocean
459 color imager (GOCI) to mapping the temporal dynamics of coastal water turbidity. *Remote Sensing of*
460 *Environment*, 146, 24-35. doi:<https://doi.org/10.1016/j.rse.2013.05.032>
- 461 Choi, J.-K., Yang, H., Han, H.-J., Ryu, J.-H., & Park, Y.-J. (2013). Quantitative estimation of suspended sediment
462 movements in coastal region using GOCI. *Journal of Coastal Research*, 165(sp2), 1367-1372.
463 doi:<https://doi.org/10.2112/SI65-231.1>
- 464 Cloern, J. E. (1987). Turbidity as a control on phytoplankton biomass and productivity in estuaries. *Continental Shelf*
465 *Research*, 7(11), 1367-1381. doi:[https://doi.org/10.1016/0278-4343\(87\)90042-2](https://doi.org/10.1016/0278-4343(87)90042-2)
- 466 Curran, P. J., Hansom, J. D., Plummer, S. E., & Pedley, M. I. (1987). Multispectral remote sensing of nearshore
467 suspended sediments: a pilot study. *International Journal of Remote Sensing*, 8(1), 103-112.
468 doi:<https://doi.org/10.1080/01431168708948618>
- 469 Doxaran, D., Froidefond, J.-M., Castaing, P., & Babin, M. (2009). Dynamics of the turbidity maximum zone in a
470 macrotidal estuary (the Gironde, France): Observations from field and MODIS satellite data. *Estuarine, Coastal*
471 *and Shelf Science*, 81(3), 321-332. doi:<https://doi.org/10.1016/j.ecss.2008.11.013>
- 472 Doxaran, D., Froidefond, J.-M., Lavender, S., & Castaing, P. (2002). Spectral signature of highly turbid waters:
473 Application with SPOT data to quantify suspended particulate matter concentrations. *Remote Sensing of*
474 *Environment*, 81(1), 149-161. doi:[https://doi.org/10.1016/S0034-4257\(01\)00341-8](https://doi.org/10.1016/S0034-4257(01)00341-8)
- 475 Fan, H., & Huang, H. (2008). Response of coastal marine eco-environment to river fluxes into the sea: A case study of
476 the Huanghe (Yellow) River mouth and adjacent waters. *Marine Environmental Research*, 65(5), 0-387.
477 doi:<https://doi.org/10.1016/j.marenvres.2008.01.003>
- 478 Gordon, H. R., Brown, J. W., & Evans, R. H. (1988). Exact Rayleigh scattering calculations for use with the Nimbus-7
479 Coastal Zone Color Scanner. *Applied Optics*, 27(5), 862-871. doi:<https://doi.org/10.1364/AO.27.000862>
- 480 He, X., Bai, Y., Pan, D., Huang, N., Dong, X., Chen, J., Chen, C.-T. A., & Cui, Q. (2013). Using geostationary satellite
481 ocean color data to map the diurnal dynamics of suspended particulate matter in coastal waters. *Remote Sensing*
482 *of Environment*, 133, 225-239. doi:<https://doi.org/10.1016/j.rse.2013.01.023>

483 Hu, C., Chen, Z., Clayton, T. D., Swarzenski, P., Brock, J. C., & Muller-Karger, F. E. (2004). Assessment of estuarine
484 water-quality indicators using MODIS medium-resolution bands: Initial results from Tampa Bay, FL. *Remote*
485 *Sensing of Environment*, 93(3), 423-441. doi:<https://doi.org/10.1016/j.rse.2004.08.007>

486 Ilyina, T., Pohlmann, T., Lammel, G., & Sündermann, J. (2006). A fate and transport ocean model for persistent organic
487 pollutants and its application to the North Sea. 63(1-2), 1-19. doi:<http://doi.org/10.1016/j.jmarsys.2006.04.007>

488 Larouche, P., & Boyer-Villemaire, U. (2010). Suspended particulate matter in the St. Lawrence estuary and Gulf surface
489 layer and development of a remote sensing algorithm. *Estuarine, Coastal and Shelf Science*, 90(4), 241-249.
490 doi:<https://doi.org/10.1016/j.ecss.2010.09.005>

491 Li, H., He, X., Ding, J., Hu, Z., Cui, W., Li, S., & Zhang, L. (2016). Validation of the remote sensing products retrieved
492 by geostationary ocean color imager in Liaodong Bay in Spring. *acta optica sinica*, 36(4).
493 doi:<http://doi.org/10.3788/AOS201636.0401002>

494 Li, J., Tian, L., Song, Q., Sun, Z., Yu, H., & Xing, Q. (2018). Temporal variation of chlorophyll-a concentrations in
495 highly dynamic waters from unattended Sensors and remote sensing observations. *Sensors (Basel, Switzerland)*,
496 18(8), 2699. doi:<https://doi.org/10.3390/s18082699>

497 Li, P., Ke, Y., Bai, J., Zhang, S., Chen, M., & Zhou, D. (2019). Spatiotemporal dynamics of suspended particulate matter
498 in the Yellow River Estuary, China during the past two decades based on time-series Landsat and Sentinel-2 data.
499 *Marine Pollution Bulletin*, 149, 110518. doi:<https://doi.org/10.1016/j.marpolbul.2019.110518>

500 Liu, Y., Huang, H., & Yang, X. (2013). The transportation and deposition of suspended sediment and its dynamic
501 mechanism analysis based on Landsat images in the Laizhou Bay. *Acta Oceanologica Sinica*, 35(6), 43-53.
502 doi:<http://doi.org/10.3969/j.issn.0253-4193.2013.06.005>

503 Luan, H., Fu, D., Li, M., Zeng, J., & Chen, Q. (2017). Based on Landsat 8 suspended sediment concentration of the
504 PearlRiver on each season inversion and analysis. *Marine environmental science*, 36(6), 892-897.
505 doi:<http://dx.doi.org/10.13634/j.cnki.mes20170615>

506 Mélin, F., Zibordi, G., & Berthon, J.-F. (2007). Assessment of satellite ocean color products at a coastal site. *Remote*
507 *Sensing of Environment*, 110(2), 192-215. doi:<https://doi.org/10.1016/j.rse.2007.02.026>

508 Mao, Z., Chen, J., Pan, D., Tao, B., & Zhu, Q. (2012). A regional remote sensing algorithm for total suspended matter in
509 the East China Sea. *Remote Sensing of Environment*, 124(124), 819-831.
510 doi:<https://doi.org/10.1016/j.rse.2012.06.014>

511 Milliman, J., & Meade, R. (1983). World wide delivery of river sediments to oceans. *The Journal of Geology*, 91(1), 1-21.
512 doi:<https://www.jstor.org/stable/30060512>

513 Mobley, C. D. (1999). Estimation of the remote-sensing reflectance from above-surface measurements. *Applied Optics*,
514 38(36), 7442-7455. doi:<https://doi.org/10.1364/AO.38.007442>

515 Olmanson, L. G., Brezonik, P. L., Finlay, J. C., & Bauer, M. E. (2016). Comparison of Landsat 8 and Landsat 7 for
516 regional measurements of CDOM and water clarity in lakes. *Remote Sensing of Environment*, 185, 119-128.
517 doi:<https://doi.org/10.1016/j.rse.2016.01.007>

518 Pan, Y., Shen, F., & Wei, X. (2018). Fusion of Landsat-8/OLI and GOCI data for hourly mapping of suspended
519 particulate matter at high spatial resolution: A case study in the Yangtze (Changjiang) Estuary. *Remote Sensing*,
520 10(2), 158. doi:<https://doi.org/10.3390/rs10020158>

521 Pang, J., Jiang, M., & Fulin, L. I. (2000). Changes and development trend of runoff, sediment discharge and coastline of
522 the yellow river estuary. *Transaction of Oceanology & Limnology*, 4.

523 Pei, W., Yao, S., Dong, S., Knight, J. F., Xu, C., & Chen, Y. (2015). Using field spectral measurements to estimate
524 chlorophyll-a in waterlogged areas of Huainan, China. *GIScience & Remote Sensing*, 52(6), 660-679.
525 doi:<http://doi.org/10.1080/15481603.2015.1082173>

526 Petus, C., Chust, G., Gohin, F., Doxaran, D., Froidefond, J.-M., & Sagarminaga, Y. (2010). Estimating turbidity and total

527 suspended matter in the Adour River plume (South Bay of Biscay) using MODIS 250-m imagery. *Continental*
528 *Shelf Research*, 30(5), 379-392. doi:<https://doi.org/10.1016/j.csr.2009.12.007>

529 Qing, S., Hao, Y., & Bao, Y. (2019). Retrieval of inorganic suspended particle size with Landsat-8 OLI data in the Yellow
530 River Estuary. *Journal of Coastal Research*, 90, 19. doi:<https://doi.org/10.2112/SI90-003.1>

531 Qing, S., Zhang, J., Cui, T., & Bao, Y. (2014). Remote sensing retrieval of inorganic suspended particle size in the Bohai
532 Sea. *Continental Shelf Research*, 73, 64-71. doi:<https://doi.org/10.1016/j.csr.2013.11.020>

533 Qiu, Z. (2013). A simple optical model to estimate suspended particulate matter in Yellow River Estuary. *Optics Express*,
534 21(23), 27891-27904. doi:<https://doi.org/10.1364/OE.21.027891>

535 Qiu, Z., Xiao, C., Perrie, W., Sun, D., Wang, S., Shen, H., Yang, D., & He, Y. (2017). Using Landsat 8 data to estimate
536 suspended particulate matter in the Yellow River estuary. *Journal of Geophysical Research: Oceans*, 122(1),
537 276-290. doi: <https://doi.org/10.1002/2016JC012412>

538 Ritchie, J. C., Zimba, P. V., & Everitt, J. H. (2003). Remote sensing techniques to assess water quality. *Photogrammetric*
539 *Engineering & Remote Sensing*, 69(6), 695-704. doi:<https://doi.org/10.14358/PERS.69.6.695>

540 Ruddick, K., Vanhellefont, Q., Yan, J., Neukermans, G., Wei, G., & Shang, S. (2012). Variability of suspended
541 particulate matter in the Bohai Sea from the geostationary Ocean Color Imager (GOCI). *Ocean Science Journal*,
542 47(3), 331-345. doi:<http://doi.org/10.1007/s12601-012-0032-4>

543 Shang, D., & Xu, H. (2018). Qualitative dynamics of suspended particulate matter in the Changjiang Estuary from
544 geostationary ocean color images: An empirical, regional modeling approach. *Sensors*, 18(12), 4186.
545 doi:<https://doi.org/10.3390/s18124186>

546 Shi, W., & Wang, M. (2012). Satellite views of the Bohai Sea, Yellow Sea, and East China Sea. *Progress in*
547 *Oceanography*, 104, 30-45. doi:<https://doi.org/10.1016/j.pocean.2012.05.001>

548 Su, J., & Wang, K. (1989). Changjiang river plume and suspended sediment transport in Hangzhou Bay. *Continental*
549 *Shelf Research*, 9(1), 93-111. doi:[https://doi.org/10.1016/0278-4343\(89\)90085-X](https://doi.org/10.1016/0278-4343(89)90085-X)

550 Sun, S., Xu, J., Li, G., Liu, X., Qiao, L., & Zhou, S. (2020). Analysis of suspended sediments concentration in the Bohai
551 Bay in winter based on remote sensing *Oceanologia et Limnologia Sinica*, 51(02), 258-264.
552 doi:<http://doi.org/10.11693/hyhz20190700151>

553 Vanhellefont, Q., & Ruddick, K. (2014). Turbid wakes associated with offshore wind turbines observed with Landsat 8.
554 *Remote Sensing of Environment*, 145, 105-115. doi:<https://doi.org/10.1016/j.rse.2014.01.009>

555 Vanhellefont, Q., & Ruddick, K. (2015). Advantages of high quality SWIR bands for ocean colour processing:
556 Examples from Landsat-8. *Remote Sensing of Environment*, 161, 89-106.
557 doi:<https://doi.org/10.1016/j.rse.2015.02.007>

558 Wang, H., Wu, X., Bi, N., Li, S., Yuan, P., Wang, A., Syvitski, J. P. M., Saito, Y., Yang, Z., Liu, S., & Nittrouer, J. (2017).
559 Impacts of the dam-orientated water-sediment regulation scheme on the lower reaches and delta of the Yellow
560 River (Huanghe): A review. *Global and Planetary Change*, 157, 93-113.
561 doi:<https://doi.org/10.1016/j.gloplacha.2017.08.005>

562 Wang, M. (2005). A refinement for the Rayleigh radiance computation with variation of the atmospheric pressure.
563 *International Journal of Remote Sensing*, 26(24), 5651-5663. doi:<https://doi.org/10.1080/01431160500168793>

564 Wang, M., & Gordon, H. R. (1994). A simple, moderately accurate, atmospheric correction algorithm for SeaWiFS.
565 *Remote Sensing of Environment*, 50(3), 231-239. doi:[https://doi.org/10.1016/0034-4257\(94\)90073-6](https://doi.org/10.1016/0034-4257(94)90073-6)

566 Wang, W., & Jiang, W. (2008). Study on the seasonal variation of the suspended sediment distribution and transportation
567 in the East China Seas based on SeaWiFS data. *Journal of Ocean University of China*, 7(4), 385-392.
568 doi:<http://doi.org/10.1007/s11802-008-0385-6>

569 Wei, Y., Jiao, J., Zhao, G., Zhao, H., He, Z., & Mu, X. (2016). Spatial-temporal variation and periodic change in
570 streamflow and suspended sediment discharge along the mainstream of the Yellow River during 1950-2013.

- 571 CATENA, 140, 105-115. doi:<https://doi.org/10.1016/j.catena.2016.01.016>
- 572 Wiseman, W. J., Fan, Y. B., Bornhold, B. D., Keller, G. H., Su, Z. Q., Prior, D. B., Yu, Z. X., Wright, L. D., Wang, F. Q.,
573 & Qian, Q. Y. (1986). Suspended sediment advection by tidal currents off the Huanghe (Yellow River) delta.
574 *Geo-Marine Letters*, 6(2), 107-113. doi:<http://doi.org/10.1007/BF02281646>
- 575 Wu, G., Liu, L., Chen, F., & Fei, T. (2014). Developing MODIS-based retrieval models of suspended particulate matter
576 concentration in Dongting Lake, China. *International Journal of Applied Earth Observation and*
577 *Geoinformation*, 32, 46-53. doi:<https://doi.org/10.1016/j.jag.2014.03.025>
- 578 Yang, D., Yin, B., Liu, Z., & Feng, X. (2011). Numerical study of the ocean circulation on the East China Sea shelf and a
579 Kuroshio bottom branch northeast of Taiwan in summer. *Journal of Geophysical Research*, 116.
580 doi:<http://doi.org/10.1029/2010JC006777>
- 581 Yu, Y., Wang, H., Shi, X., Ran, X., Cui, T., Qiao, S., & Liu, Y. (2013). New discharge regime of the Huanghe (Yellow
582 River): Causes and implications. *Continental Shelf Research*, 69, 62-72.
- 583 Zhang, M., Tang, J., Dong, Q., Song, Q., & Ding, J. (2010). Retrieval of total suspended matter concentration in the
584 Yellow and East China Seas from MODIS imagery. *Remote Sensing of Environment*, 114(2), 392-403.
585 doi:<https://doi.org/10.1016/j.rse.2009.09.016>
- 586 Zhang, M. W., Dong, Q., Cui, T. W., Xue, C. J., & Zhang, S. L. (2014). Suspended sediment monitoring and assessment
587 for Yellow River estuary from Landsat TM and ETM plus imagery. *Remote Sensing of Environment*, 146,
588 136-147. doi:<http://doi.org/10.1016/j.rse.2013.09.033>
- 589 Zhang, Y., Lin, S., Liu, J., Qian, X., & Ge, Y. (2010). Time-series MODIS image-based retrieval and distribution analysis
590 of total suspended matter concentrations in Lake Taihu (China). *International Journal of Environmental*
591 *Research and Public Health*, 7(9). doi:<http://doi.org/10.3390/ijerph7093545>
- 592 Zhao, W., Sun, L., Cui, T., Cao, W., Ma, Y., & Hao, Y. (2014). Mapping the distribution of suspended particulate matter
593 concentrations influenced by storm surge in the Yellow River Estuary using FY-3A MERSI 250-m data. *Aquatic*
594 *Ecosystem Health & Management*, 17(3), 290-298. doi:<http://doi.org/10.1080/14634988.2014.944821>

595 **Declarations**

596 Availability of data and materials

597 Please contact author for data requests.

598 Acknowledgement

599 We thank the anonymous reviewers and the editor for their constructive and valuable comments that helped
600 improve the manuscript further.

601 Funding

602 This work was funded by the Science and Technology Major Project on Lakes of Inner Mongolia (Grant No.
603 ZDZX2018054), National Natural Science Foundation of China (Grant No. 51869014, 61461034), Inner
604 Mongolian Natural Science Foundation of China (Grant No. 2019MS03023), Key Scientific and Technological
605 Project of Inner Mongolia (Grant No. 2019GG019)

606 Authors' contributions

607 JL participated in the data analysis and research idea design and completed the main work of the paper. YLH
608 participated in its design and coordination. ZZZ participated in the data analysis and drafted the manuscript. ZPL
609 participated in the data analysis and drafted the manuscript. RYH participated in the data analysis and drafted the
610 manuscript. YS participated in the data analysis and drafted the manuscript. All authors read and approved the final
611 manuscript.

612 Competing interests

613 The authors declare that they have no competing interests.

Figures

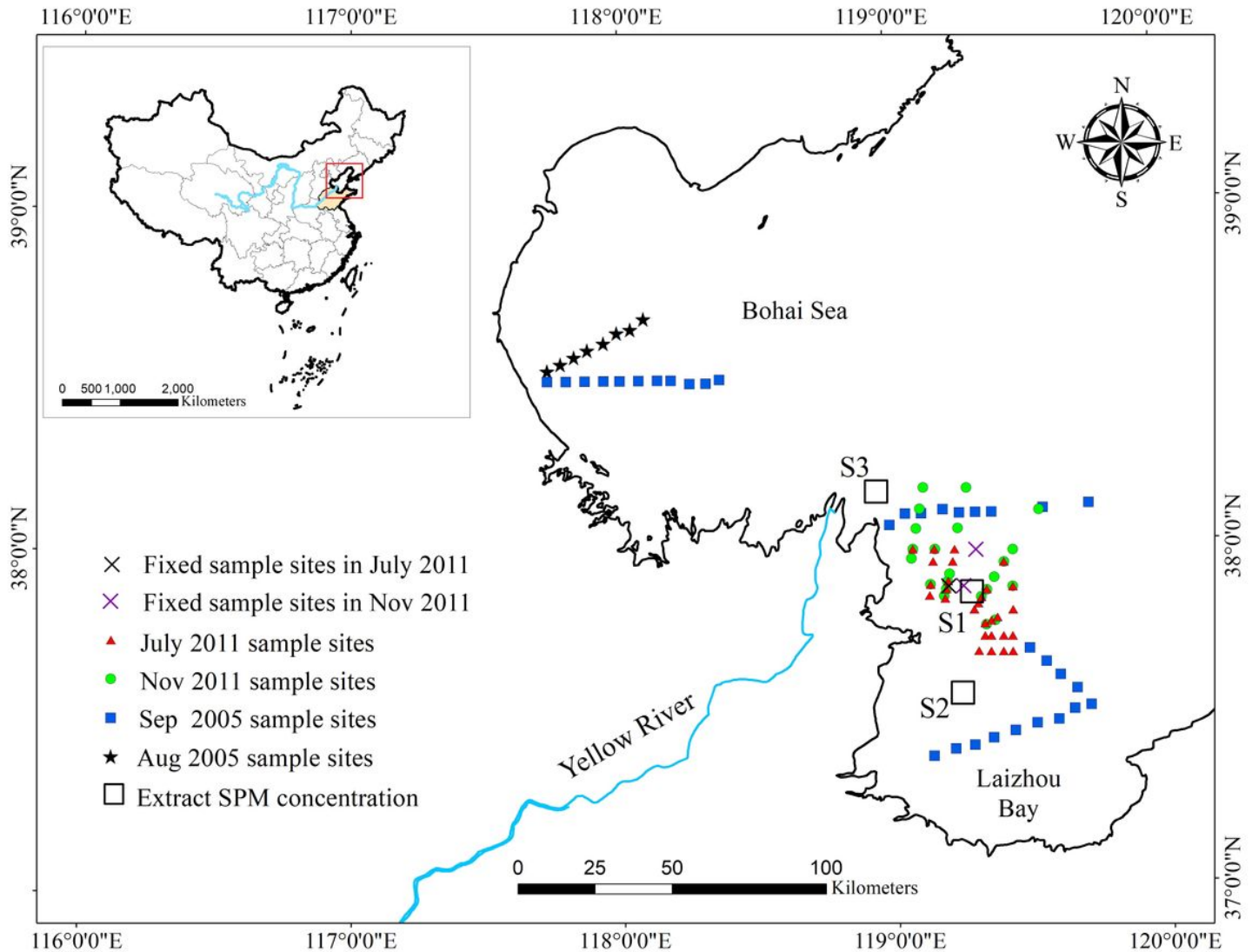


Figure 1

Sampling site map during three cruises (The red solid triangle represents sample sites in July 2011; the green solid dot represents sample sites in November 2011; the blue polygon represents sample sites in Aug 2005; the black solid star represents sample sites in Sep 2005; the cross represents three fixed sample sites (black cross represents in July 2011, and the purple cross was in Nov 2011); the black hollow square boxes of 40×40 pixels for characterizing SPM (S1, S2, S3). Note: The designations employed and the presentation of the material on this map do not imply the expression of any opinion whatsoever on the part of Research Square concerning the legal status of any country, territory, city or area or of its authorities, or concerning the delimitation of its frontiers or boundaries. This map has been provided by the authors.

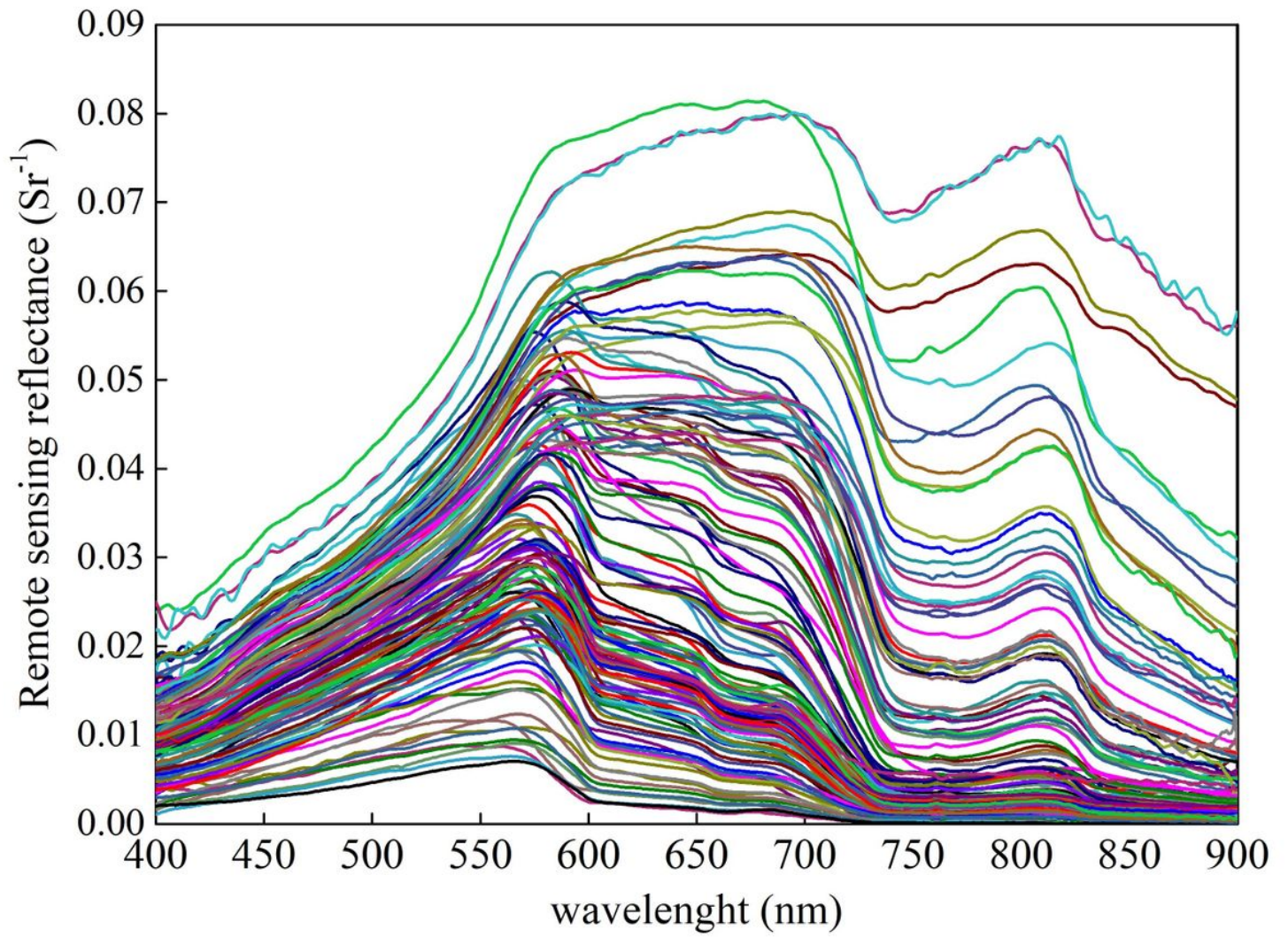


Figure 2

The remote sensing reflectance during three cruise.

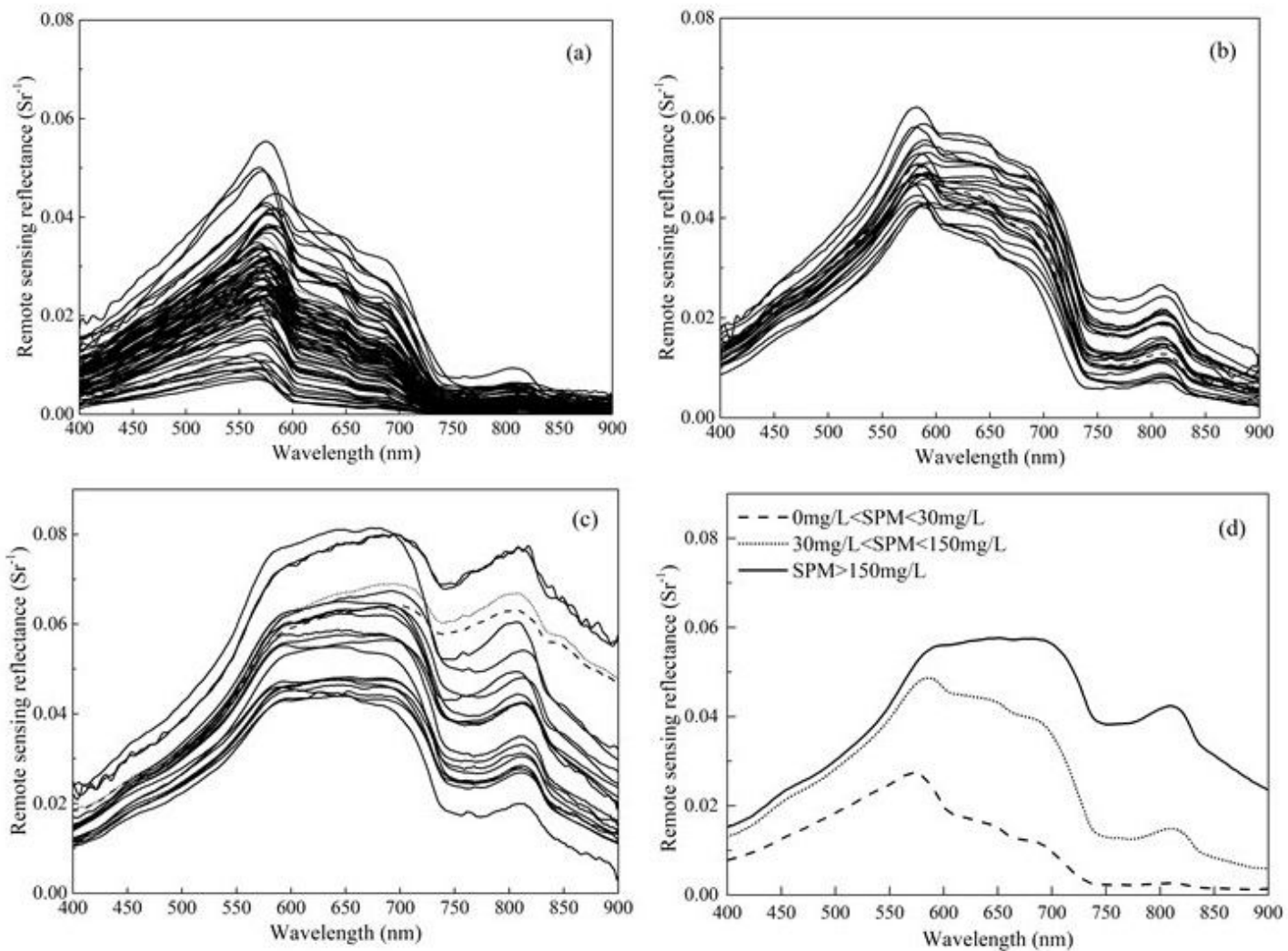


Figure 3

R_{rs} and mean R_{rs} of different SPM range. (a) R_{rs} in the low turbidity water (with $0 \text{ mg/L} < \text{SPM} < 30 \text{ mg/L}$); (b) 127 R_{rs} in the moderate turbidity water (with $30 \text{ mg/L} < \text{SPM} < 150 \text{ mg/L}$); (c) R_{rs} in the high turbidity water (with 128 $\text{SPM} > 150 \text{ mg/L}$); (d) Mean R_{rs} in three different SPM range.

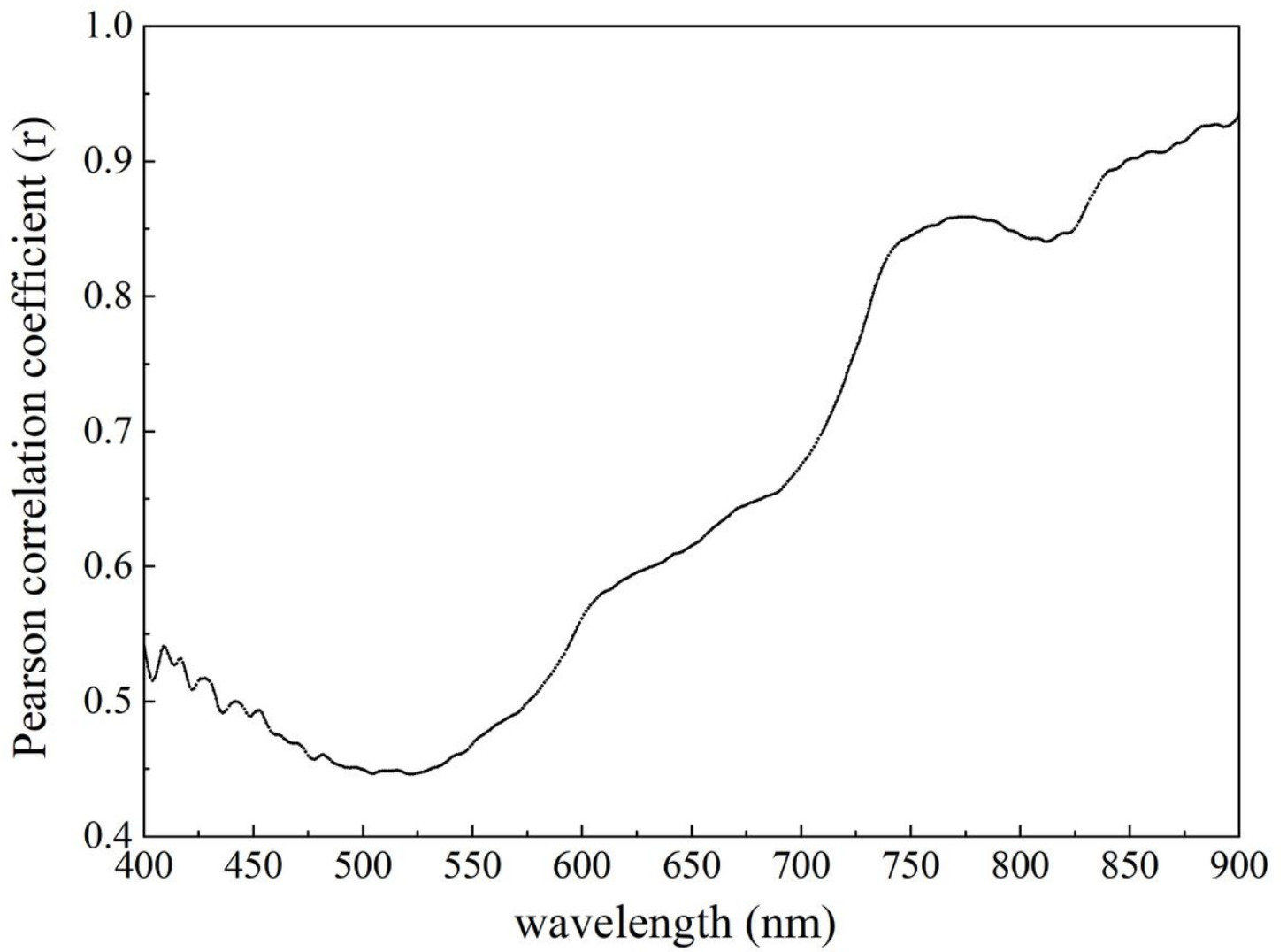


Figure 4

The correlation coefficient of the Rrs with SPM at different wavelengths.

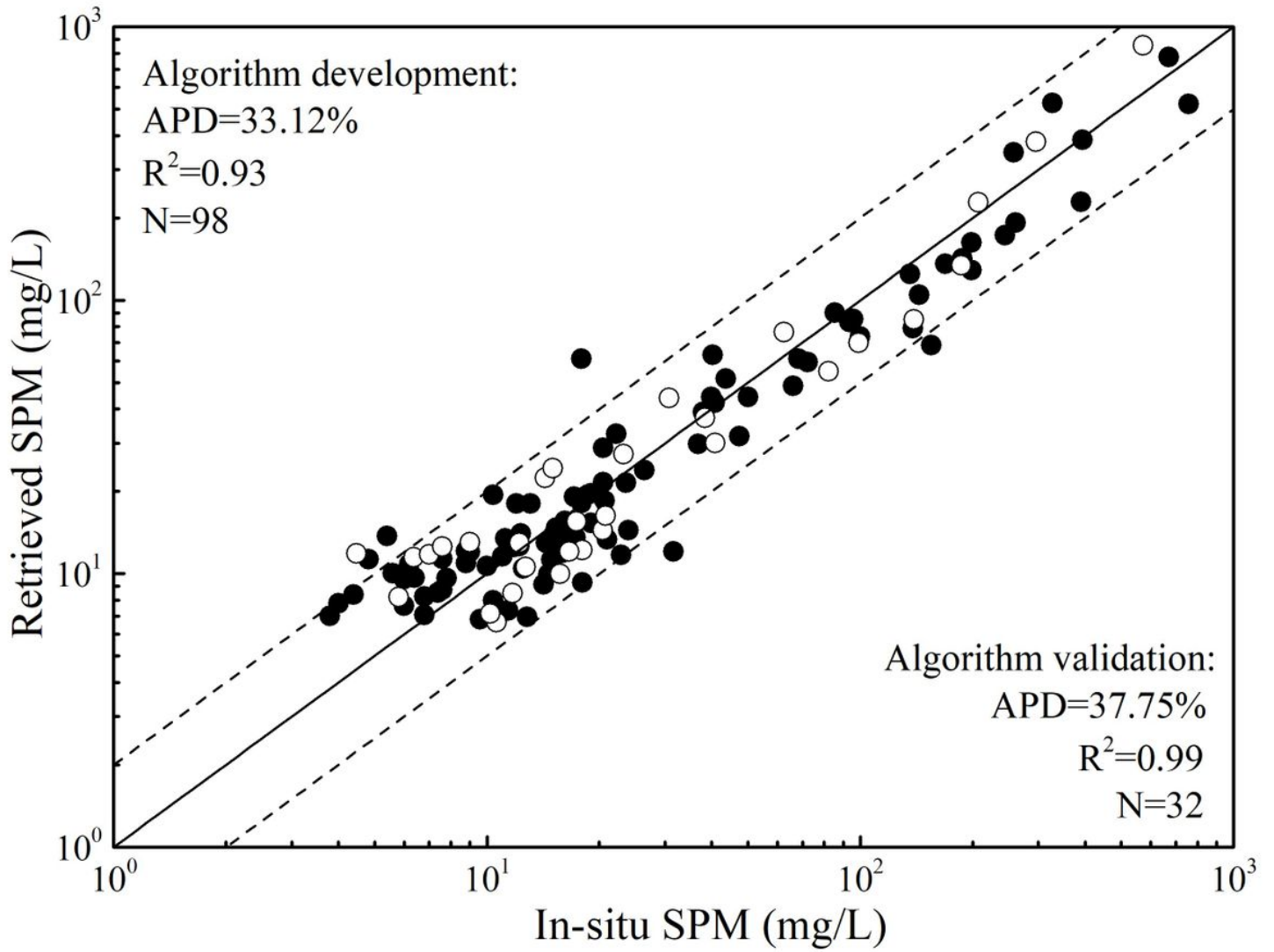


Figure 5

The scatter plot with the optimal algorithm by Landsat 8 OLI. The solid dots are used to create algorithm, and the hollow dots are used to test the algorithm.

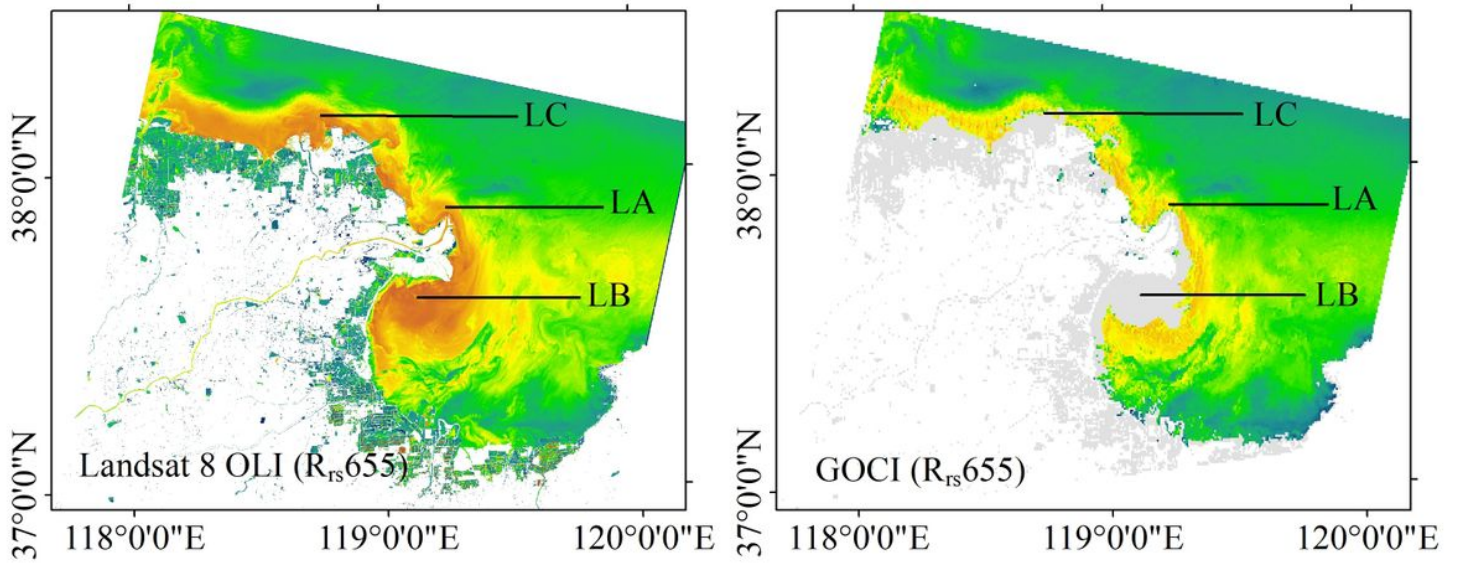


Figure 6

Landsat 8 OLI $R_{rs}(655)$ versus GOCI $R_{rs}(660)$. Gray areas denoted mask areas. Three transects (marked as LA, LB and LC) in the figure were used for the cross validation of Landsat 8 OLI measured R_{rs} and GOCI measurements.

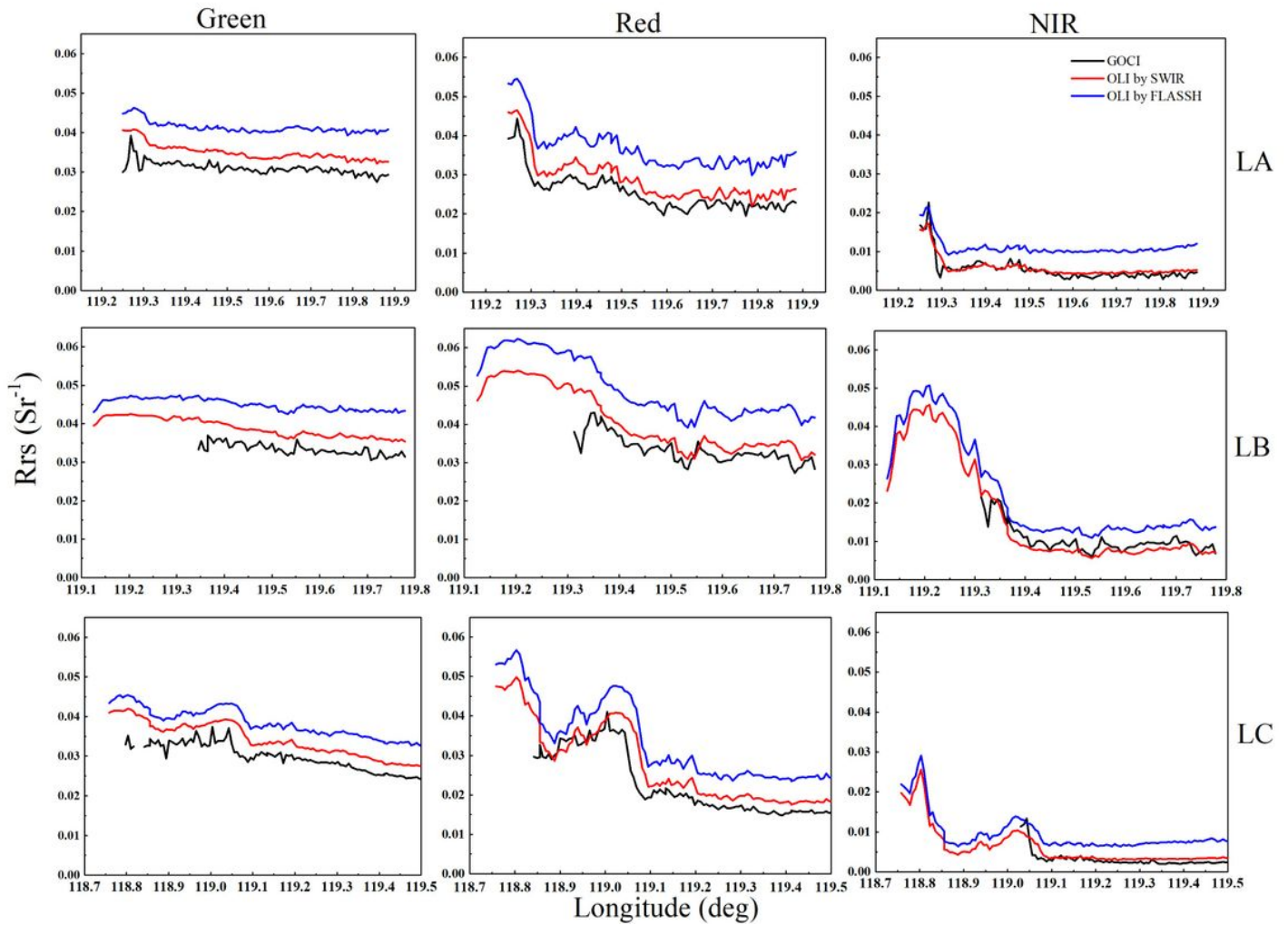


Figure 7

Comparisons of measured Rrs between Landsat 8 OLI and GOCI along three west-east transects. Three bands from left to right: Green [Landsat 8 OLI Rrs(561) versus GOCI Rrs(555)]; Red [Landsat 8 OLI Rrs(655) versus GOCI Rrs(660)]; NIR [Landsat 8 OLI Rrs(865) versus GOCI Rrs(745)]. And three transects from left to right: transects LA, LB, and LC.

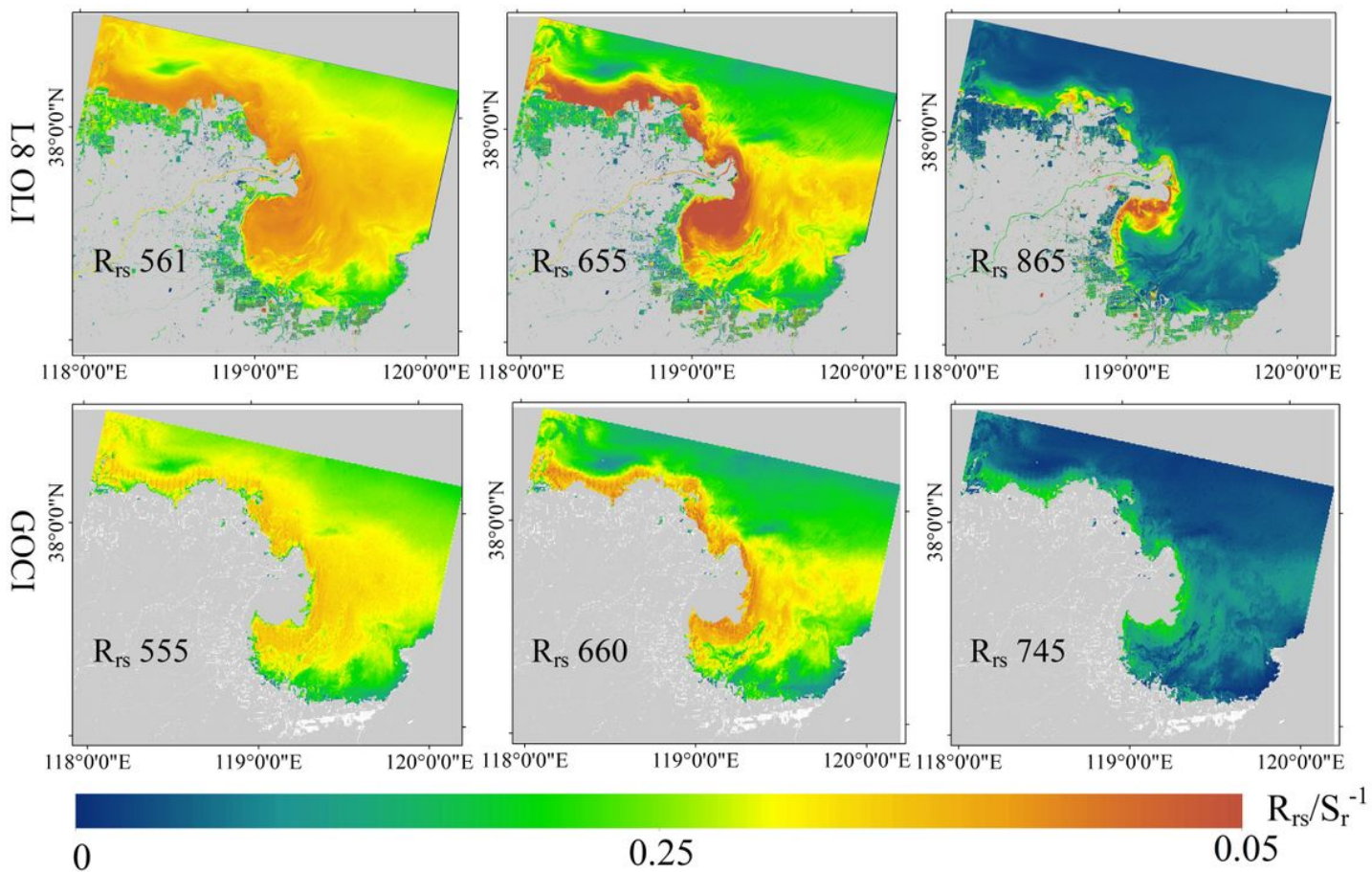


Figure 8

Comparisons of the retrieved R_{rs} between the Landsat 8 OLI and GOCI on 26 August, 2016 (The Landsat 8 OLI image was obtained at UTC 2:42, and the GOCI image was obtained at UTC 2:28).

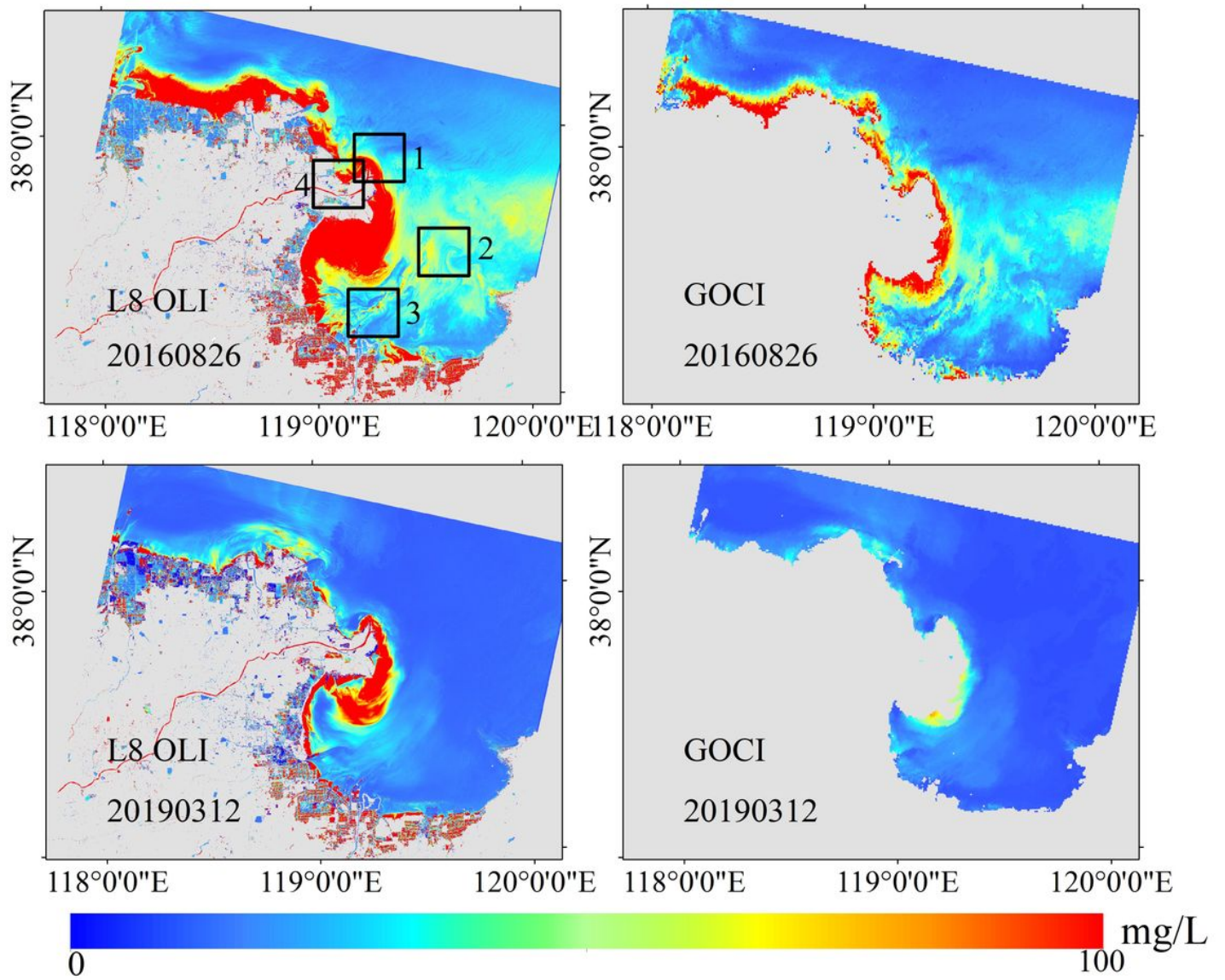


Figure 9

Comparison of the estimated SPM from Landsat 8 OLI to GOCI on 26 August 2016 and 12 March 2019.

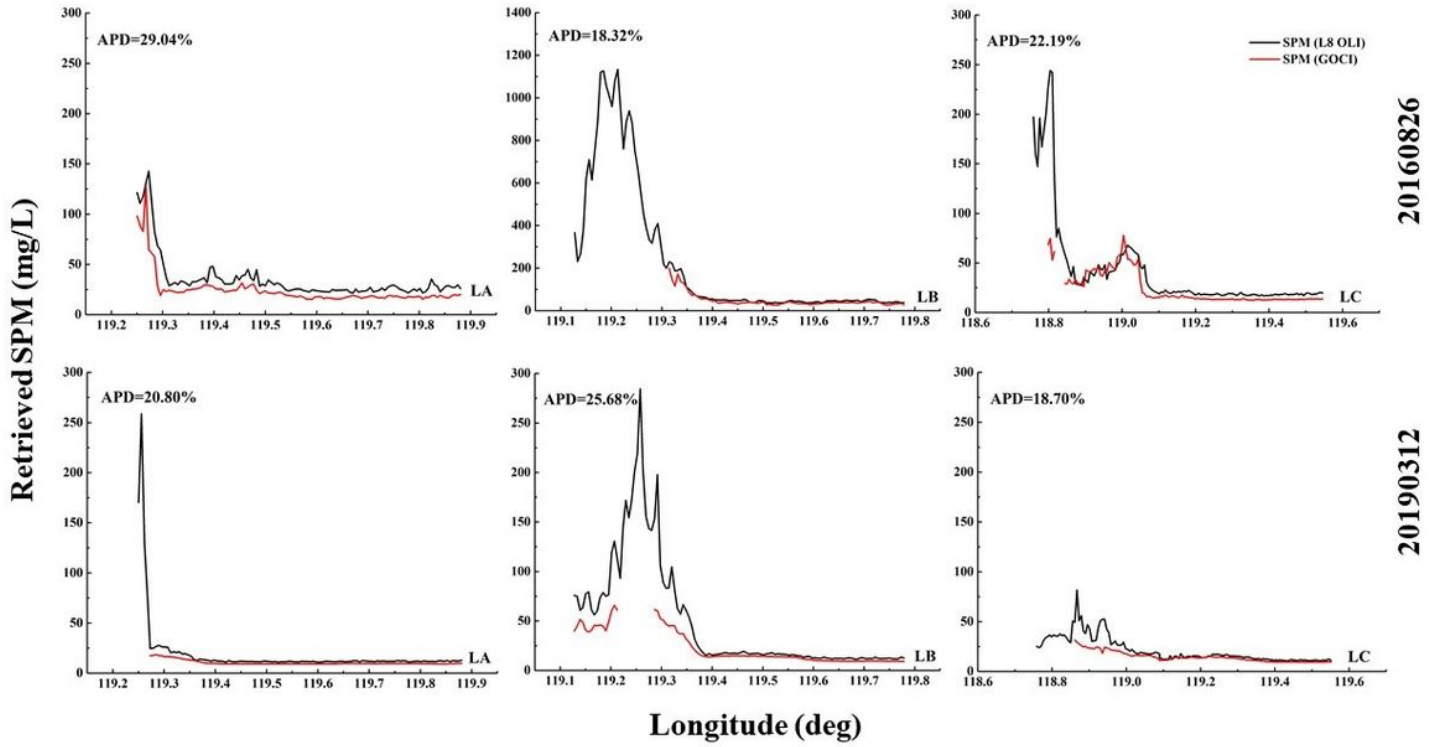


Figure 10

Comparisons between Landsat 8 OLI and GOCI derived SPM along west-east transects, and APD is the relative error between the two sensors.

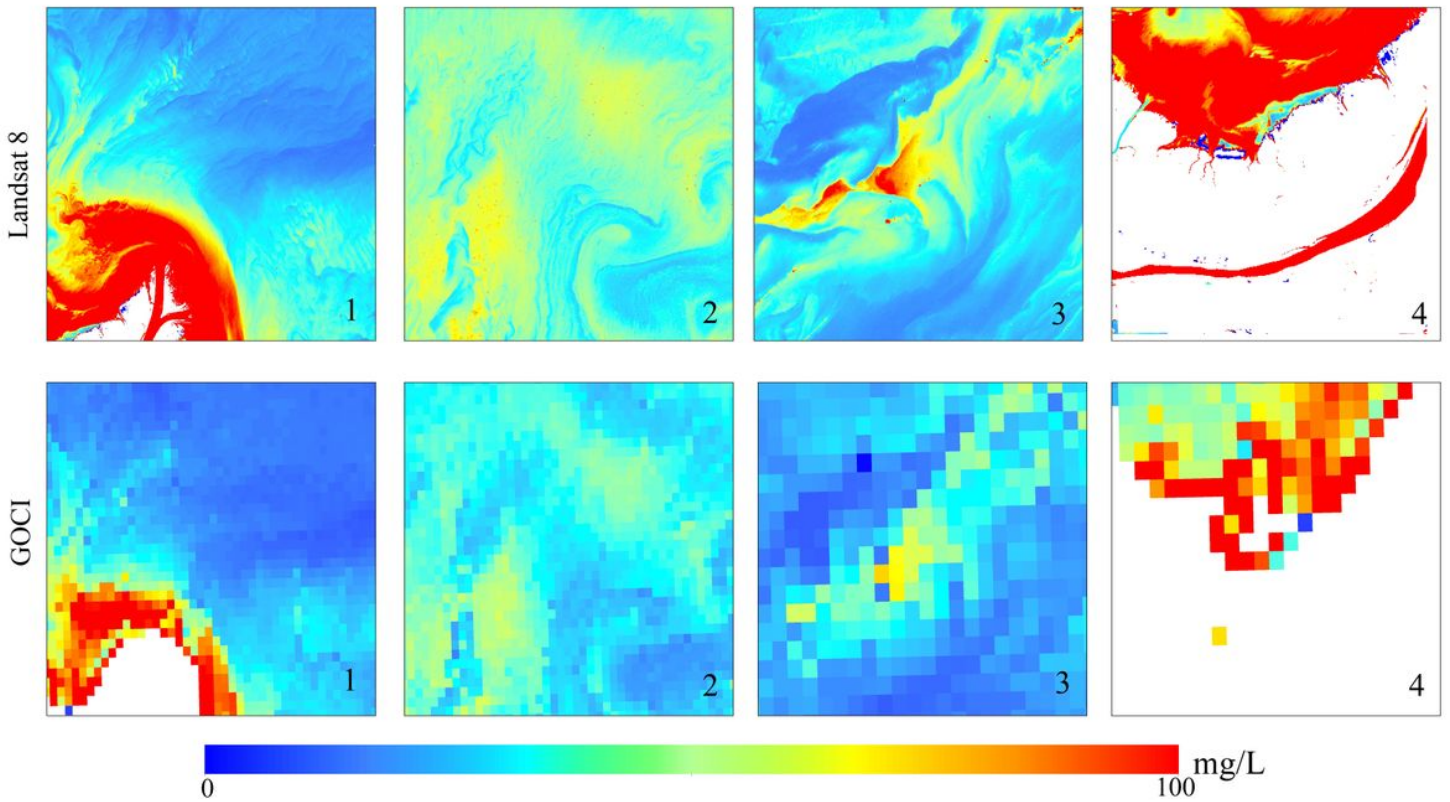


Figure 11

The details of SPM spatial distribution in four selected typical locations between Landsat 8 OLI and GOCI. The first row are the SPM distribution of Landsat 8 OLI, and the second row are GOCI.

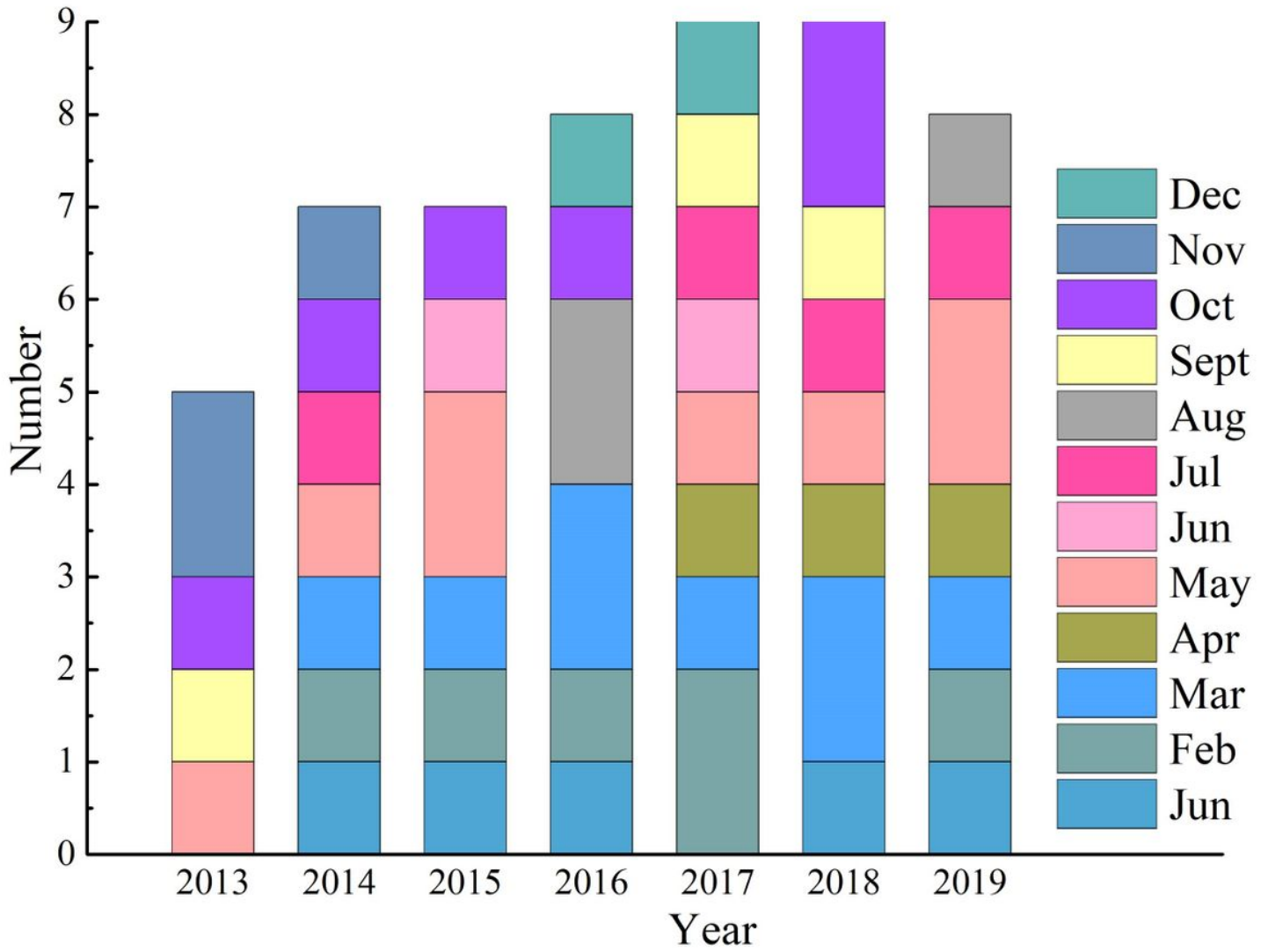


Figure 12

Images quality of this study in different months from 2013 to 2019.

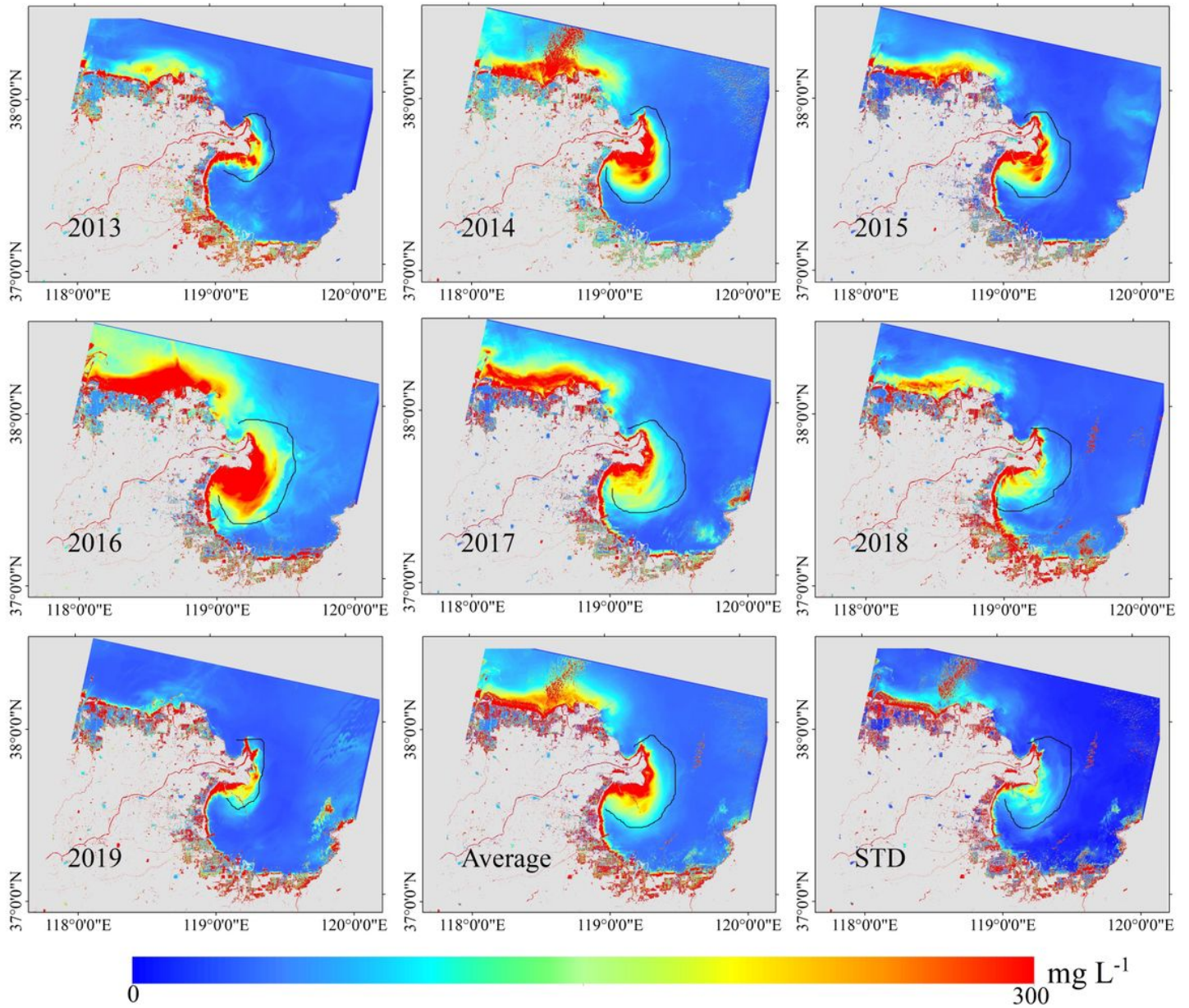


Figure 13

Distribution of the mean annual SPM and Seven-year average standard deviation retrieved by Landsat 8 OLI from 2013 to 2019.

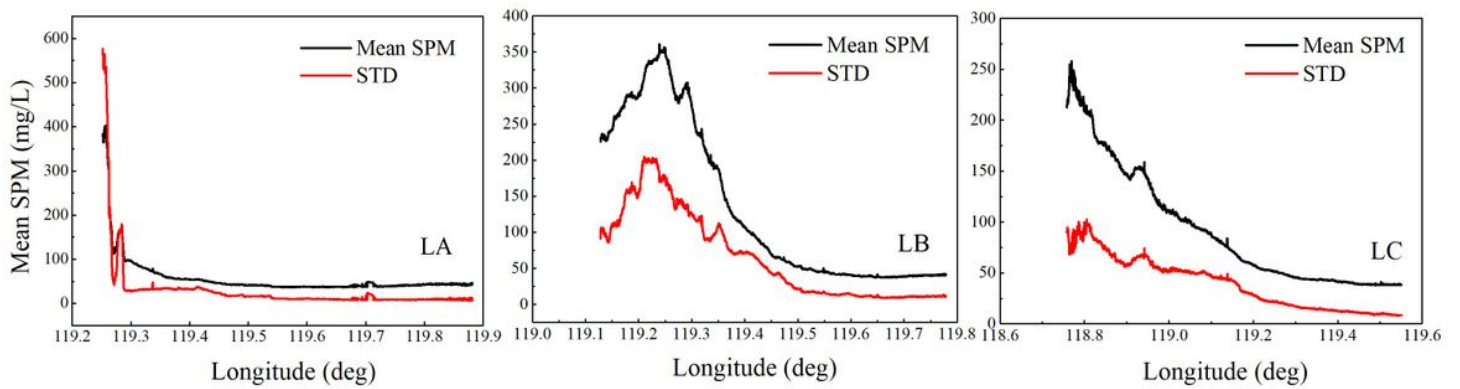


Figure 14

Comparisons between mean SPM and standard deviation (STD) along the three west-east transects in three different lines (shown in Fig. 6). Mean SPM and STD were derived from 2013 to 2019 Landsat8 OLI retrieved.

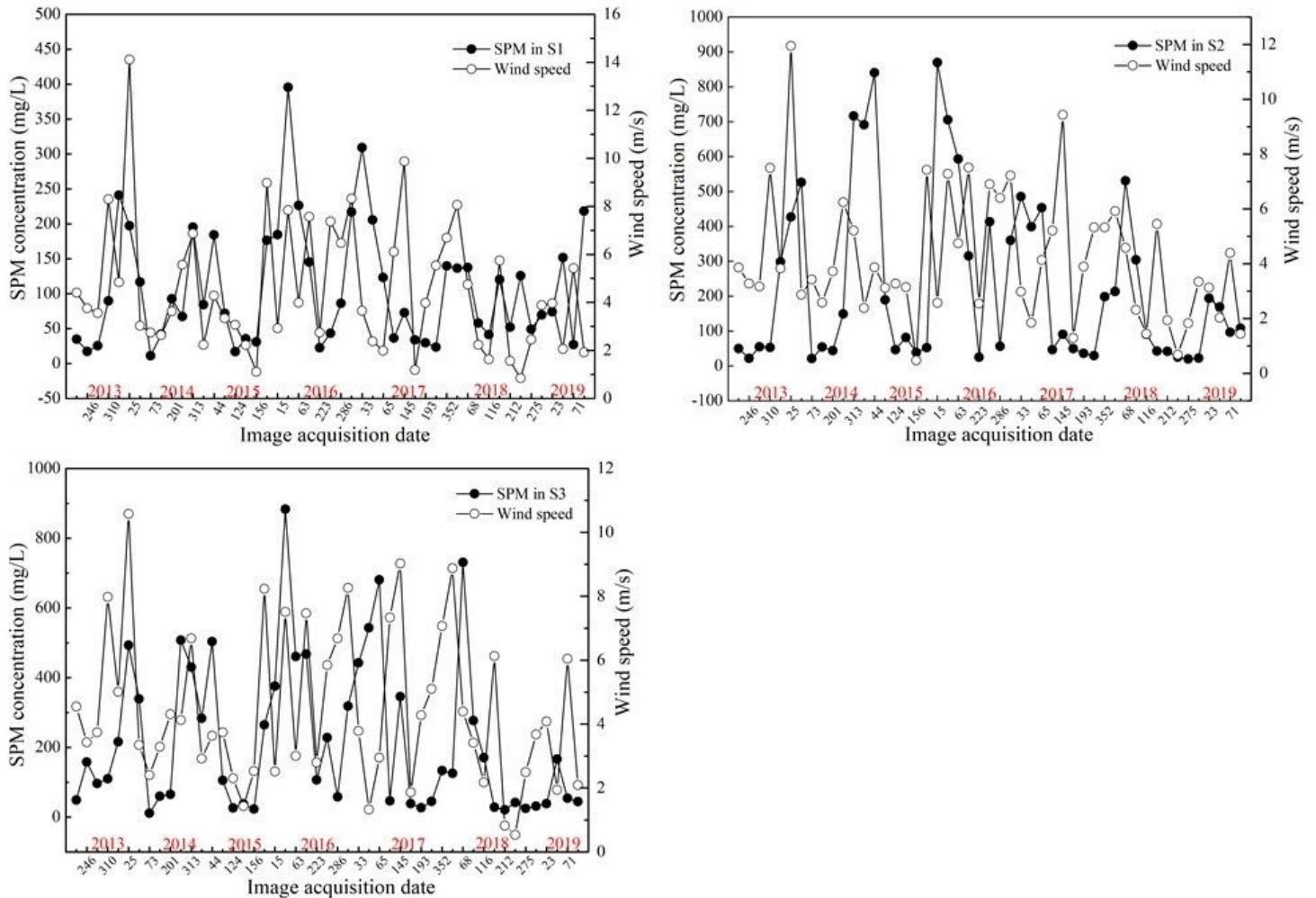


Figure 15

The relationship between SPM and wind speed in the three representative areas (S1, S2, S3). The x-axis represents the number of days in the year.

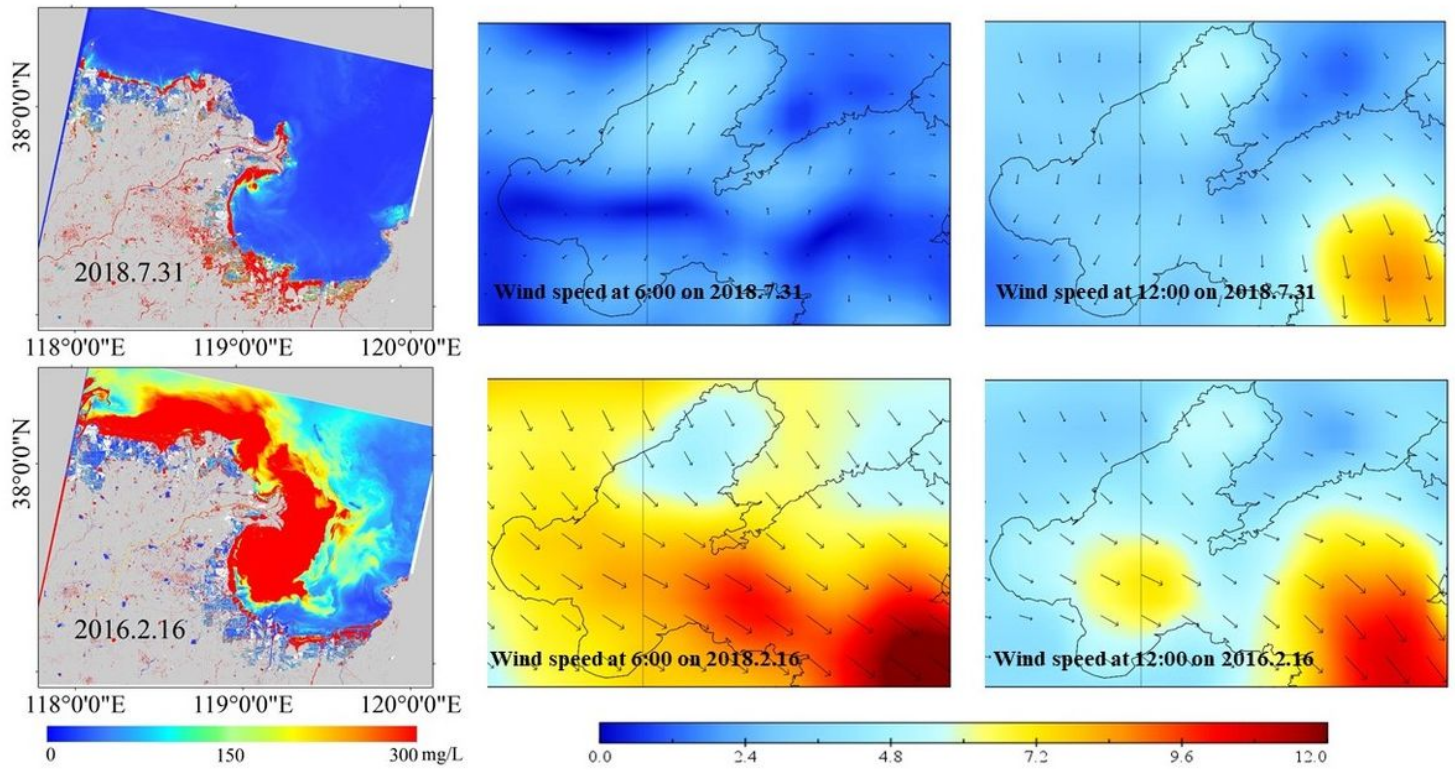


Figure 16

SPM distributions mapped by Landsat 8 OLI under different wind conditions. The images were acquired on 20160216 (Three images of the first row) with maximum wind speed 4.6m/s and on 20180731 (Three images of second row) with maximum wind speed 8.4m/s.

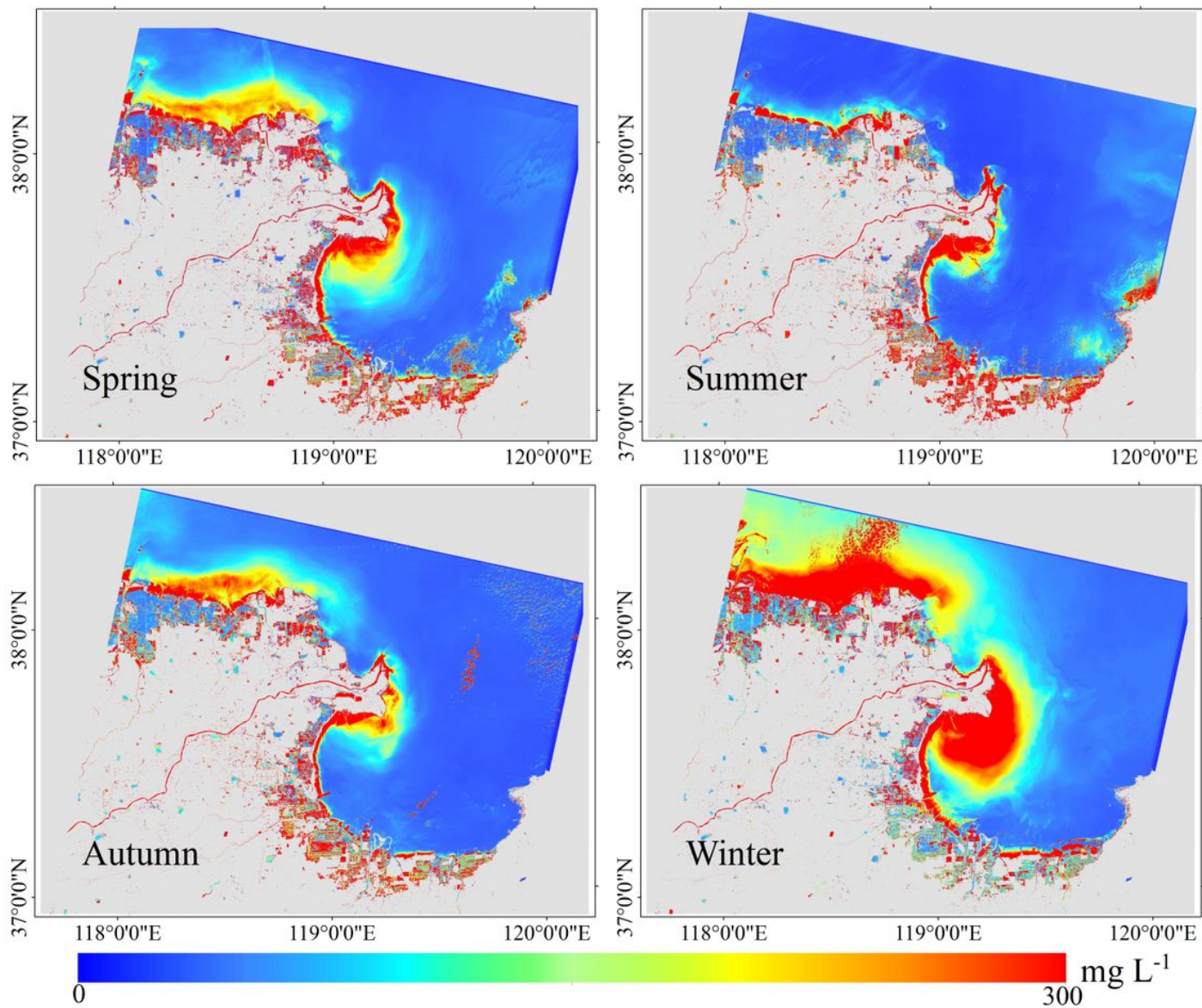


Figure 17

The mean seasonal SPM retrieved by Landsat 8 OLI from 2013 to 2019 and red range demark the maxima concentration zone.

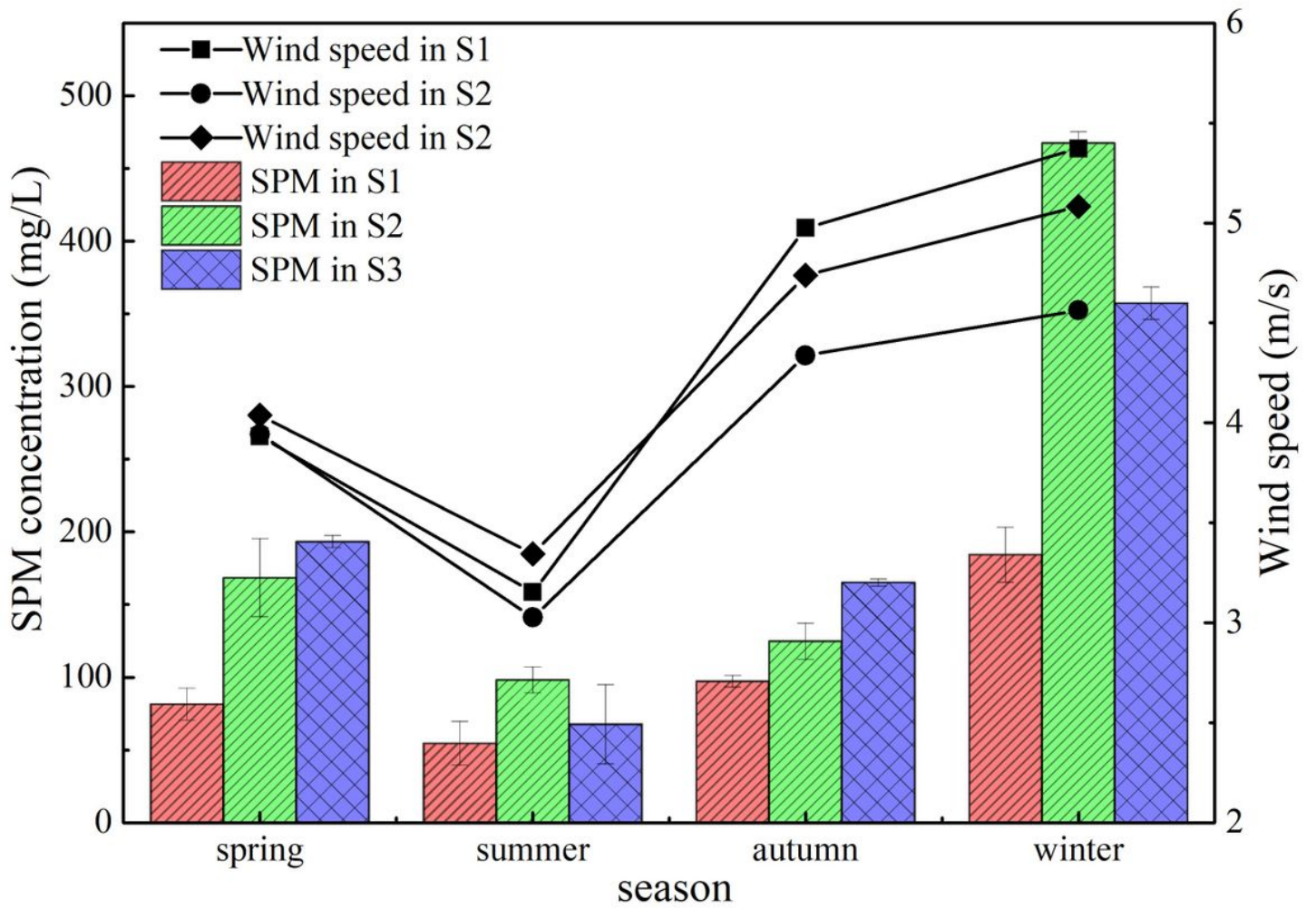


Figure 18

The variation of SPM concentration and wind speed with season.

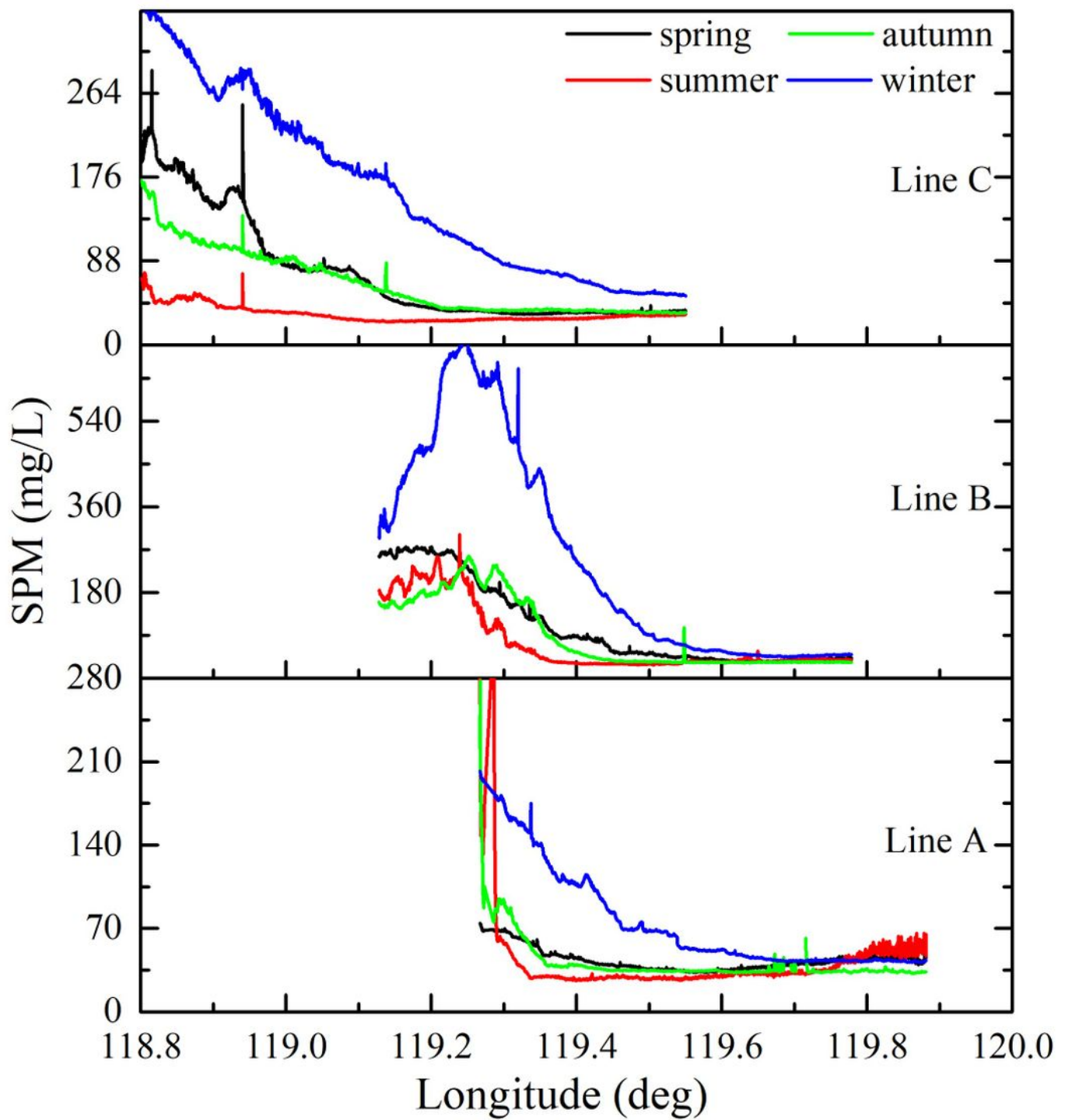


Figure 19

Comparisons between mean seasonal SPM along the three west-east transects (LA, LB and LC were shown in Fig. 6). Mean seasonal SPM were derived from 2013 to 2019 Landsat 8 OLI measurements.

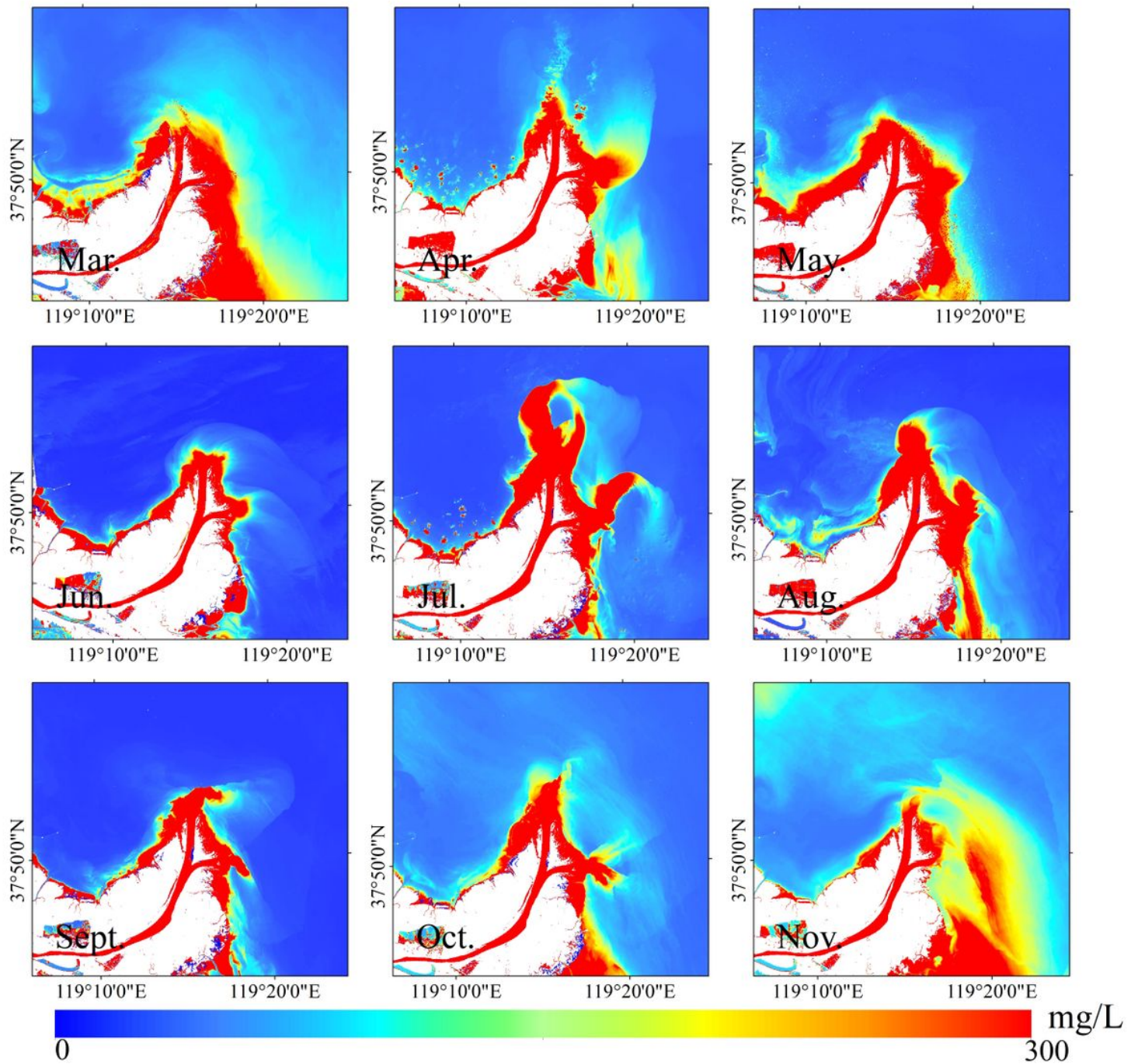


Figure 20

Monthly mean SPM maps in yellow river mouth area retrieved by Landsat 8 OLI in the YRE from 2013 to 2019.

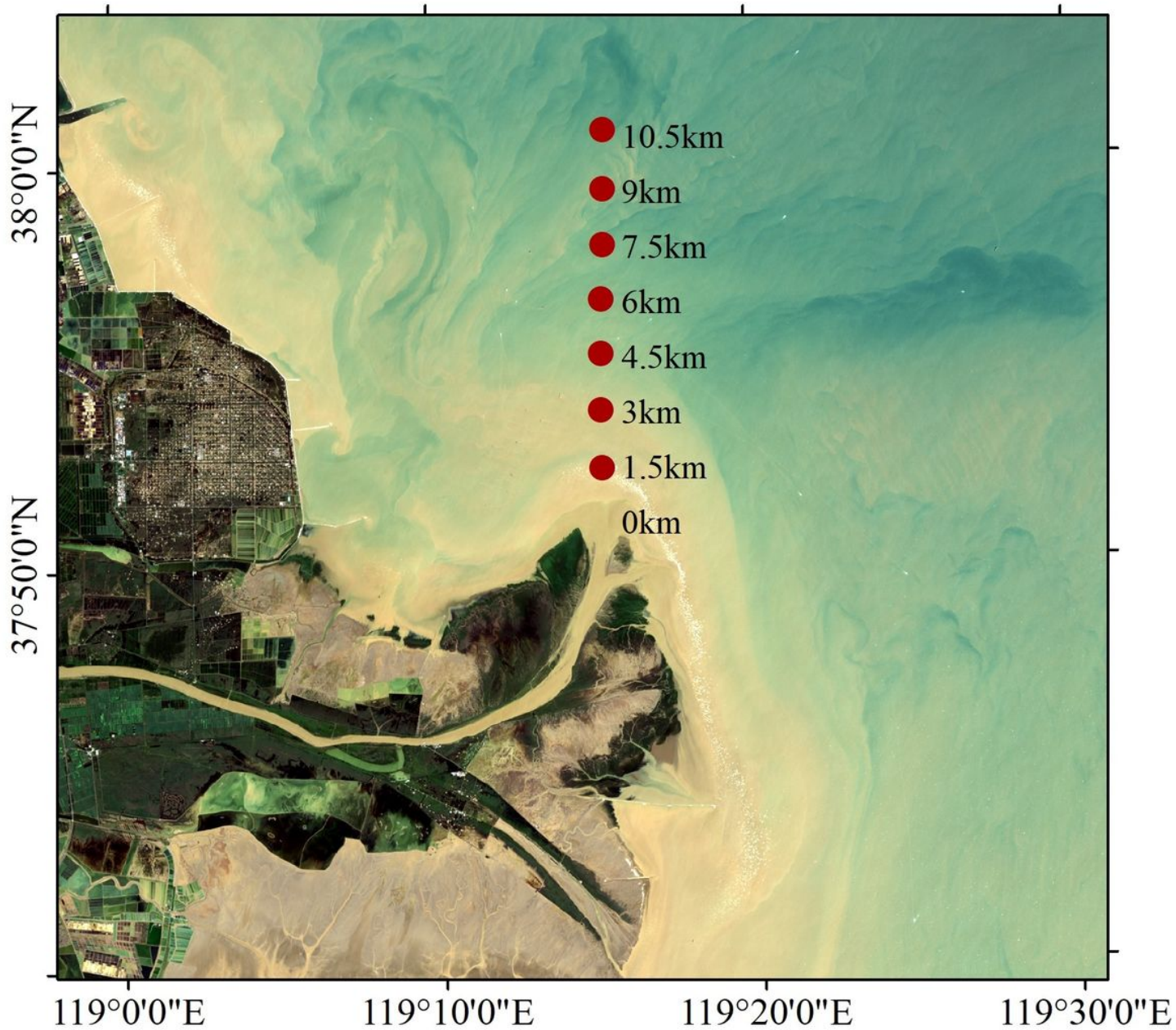


Figure 21

The location of buffers along the Yellow River direction. Note: The designations employed and the presentation of the material on this map do not imply the expression of any opinion whatsoever on the part of Research Square concerning the legal status of any country, territory, city or area or of its authorities, or concerning the delimitation of its frontiers or boundaries. This map has been provided by the authors.

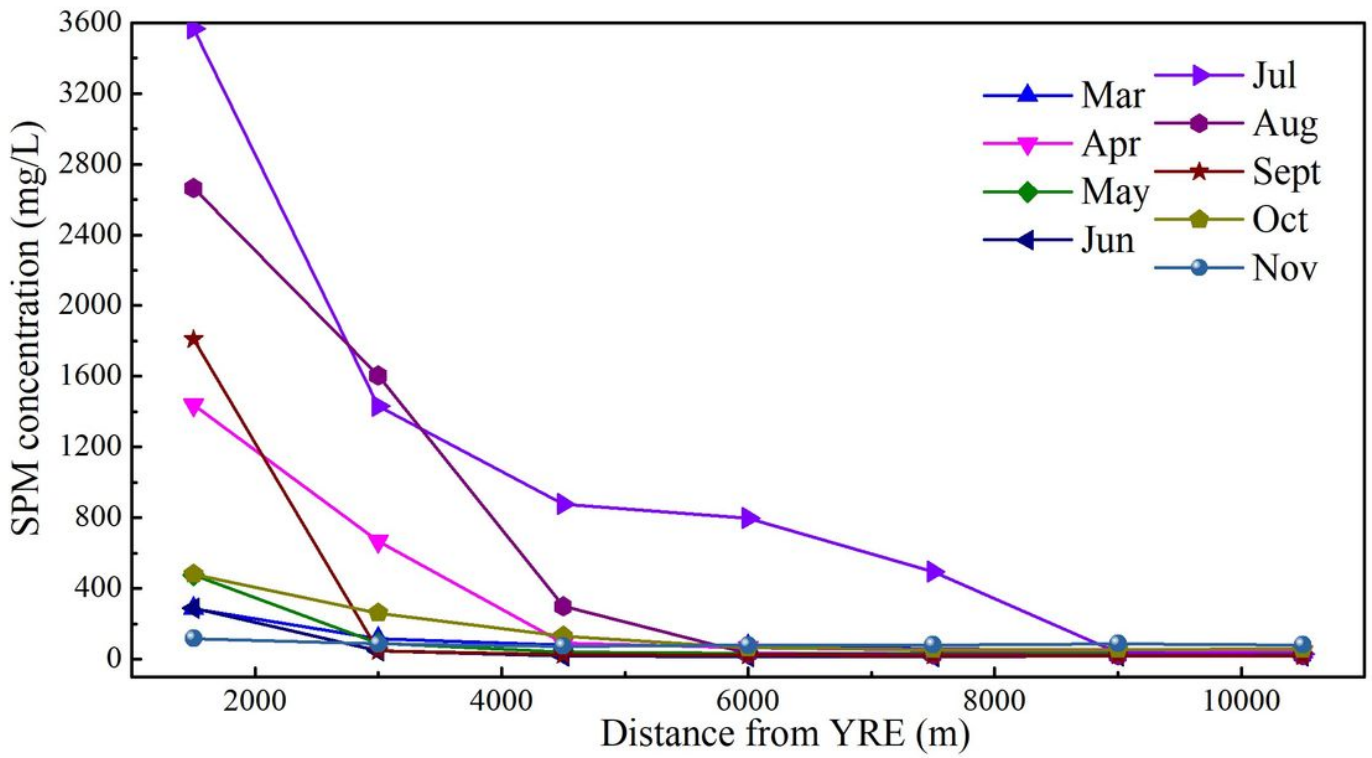


Figure 22

The variation of SPM with the distance from YRE in 12 months.

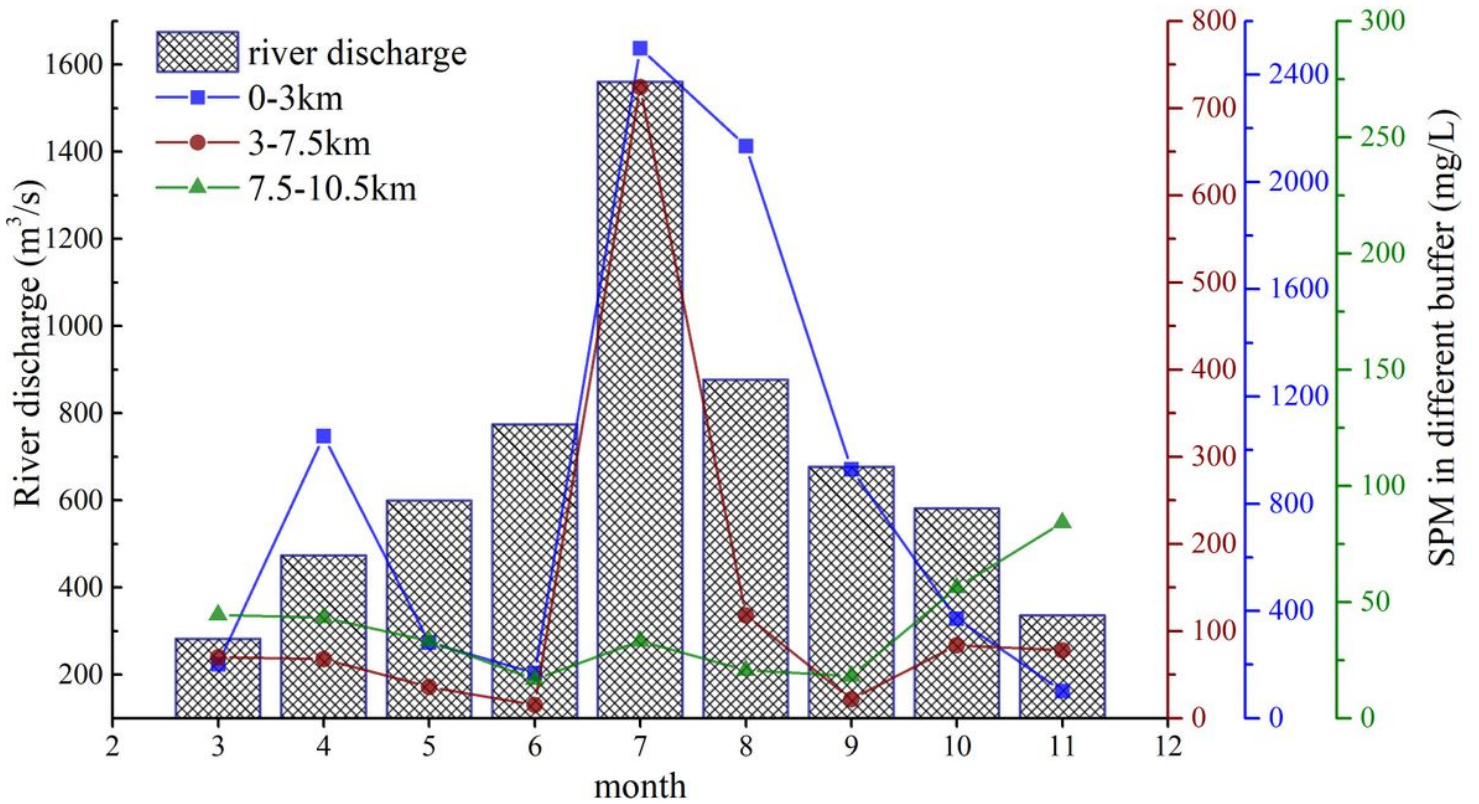


Figure 23

The monthly mean river discharge and the SPM in three redistributed buffers from 2013 to 2019. Please note the consistency of the SPM coordinate colors.